Time-Resolved Interactome Profiling Deconvolutes Secretory Protein Quality Control Dynamics

Madison T. Wright[1], Bibek Timalsina[1,2], Valeria Garcia Lopez[2], & Lars Plate[1,2,3,*]

[1]Department of Chemistry, Vanderbilt University, Nashville, TN, USA

[2]Department of Biological Sciences, Vanderbilt University, Nashville, TN, USA

[3]Lead Contact

*Correspondence: lars.plate@vanderbilt.edu

SUMMARY

Many cellular processes are governed by protein-protein interactions that require tight spatial and temporal regulation. Accordingly, it is necessary to understand the dynamics of protein interactions to fully comprehend and elucidate cellular processes and pathological disease states. To map de novo protein-protein interactions with time-resolution at an organelle-wide scale, we developed a quantitative mass-spectrometry method, time-resolved interactome profiling (TRIP). We apply TRIP to elucidate aberrant protein interaction dynamics that lead to the protein misfolding disease congenital hypothyroidism. We deconvolute altered temporal interactions of the thyroid hormone precursor thyroglobulin with pathways associated with hypothyroidism pathophysiology such as Hsp70/90 assisted folding, disulfide/redox processing, and N-glycosylation. Functional siRNA screening identified VCP and TEX264 as key protein degradation components whose inhibition selectively rescues mutant prohormone secretion. Ultimately, our results provide insight into the temporal coordination of protein homeostasis, and our TRIP method can have broad application in investigating protein folding diseases and cellular processes.

HIGHLIGHTS

- Method to map de novo protein-protein interactions with temporal resolution
- Characterization of the time-resolved interactome of a protein folding disease state

30 • siRNA screening identifies VCP and TEX264 as major regulators of thyroglobulin
31 processing
32 • VCP pharmacological inhibition rescues mutant thyroglobulin secretion
33

34 **INTRODUCTION**

35 Protein-protein interactions drive functional diversity within cells and are often closely
36 connected to the observed phenotypes for cellular processes and disease states
37 (Bludau and Aebersold, 2020). Protein homeostasis (proteostasis) is a critical cellular
38 process that relies on tightly regulated protein interactions. The proteostasis network
39 (PN), consisting of protein folding chaperones, trafficking, and degradation components,
40 maintains the integrity of the proteome by ensuring the appropriate trafficking and locali-
41 zation of properly folded proteins while recognizing misfolded, potentially detrimental
42 states and routing them for degradation (Behnke et al., 2016; Karagöz et al., 2019;
43 Needham et al., 2019; Pohl and Dikic, 2019). The concerted action of hundreds of pro-
44 teostasis factors is referred to as protein quality control (PQC). Perturbations to the pro-
45 teostasis network through genetic, age-related, or environmental factors manifest in
46 several disease states including amyloidosis, neurodegeneration, cancer, and others
47 (Kuo et al., 2021; Marinko et al., 2021; McDonald et al., 2022; Taldone et al., 2020;
48 Wright et al., 2021).

49 Identifying and quantifying protein-protein interactions has been critical for com-
50 prehending the pathogenesis of these disease states. Approaches include yeast two-
51 hybrid systems, co-immunoprecipitation coupled with western blot analysis,

52 Luminescence-based Mammalian IntERactome (LUMIER) assay, as well as affinity pu-
53 rification – mass spectrometry (AP-MS) (Piette et al., 2021; Rizzolo and Houry, 2019;
54 Rizzolo et al., 2017; Taipale et al., 2012, 2014; Wright and Plate, 2021). These methods
55 have been powerful for mapping steady-state proteostasis interactions to disease
56 states, yet most lack the ability to measure interaction dynamics over time. Proximity la-
57 beling mass spectrometry (BioID & APEX-MS) has had limited use to spatiotemporally
58 resolve protein-protein interactions only following protein maturation, as synchronization
59 of newly synthesized protein populations is challenging to achieve (Lobingier et al.,
60 2017; Perez Verdaguer et al., 2022). Unnatural amino acid incorporation methods, such
61 as biorthogonal non-canonical amino acid tagging (BONCAT), pulsed azidohomo-
62 alanine (PALM), or heavy isotope labeled azidohomoalanine (HILAQ) can identify newly
63 synthesized proteins but have not focused on a single endogenously expressed protein
64 or group of proteins in the context of disease (Bagert et al., 2014; van Bergen et al.,
65 2021; Dieterich et al., 2006; Howden et al., 2013; Ma et al., 2017, 2018; McClatchy et
66 al., 2015).
67 Similar DNA and RNA labeling approaches are used to temporally resolve nas-
68 cent DNA-protein and RNA-protein interactions in cell culture and whole organisms. Iso-
69 lation of proteins on nascent DNA (iPOND) has revealed the timing of DNA-protein in-
70 teractions during replication and chromatin assembly (Cortez, 2017; Munden et al.,
71 2022; Sirbu et al., 2011). Thiouracil crosslinking mass spectrometry (TUX-MS) and viral
72 cross-linking and solid-phase purification (VIR-CLASP) are used to study the timing of
73 RNA-protein interactions during viral infection (Kim et al., 2020; Phillips et al., 2016). In

74 contrast, no methods were previously available to identify de novo protein-protein inter-
75 actions of newly synthesized proteins in a client specific manner with temporal resolu-
76 tion, which has motivated our efforts here.

77 In earlier work, we mapped the interactome of the secreted thyroid prohormone
78 thyroglobulin (Tg), comparing the WT protein to secretion-defective mutations impli-
79 cated in congenital hypothyroidism (CH) (Wright et al., 2021). Tg is a heavily post-trans-
80 lationally modified, 330 kDa prohormone that is necessary to produce triiodothyronine
81 (T3) and thyroxine (T4) thyroid specific hormones. Tg biogenesis relies extensively on
82 distinct interactions with the PN to facilitate folding and eventual secretion (Citterio et
83 al., 2019; Coscia et al., 2020). Our previous results identified topological changes in Tg-
84 PN interactions among CH-associated Tg mutants compared to WT. Nonetheless, the
85 lack of temporal resolution precludes more mechanistic discernment of these changes
86 in PN interactions. While some changes may simply correlate with disease pathogene-
87 sis, others may be directly responsible for the aberrant PQC and secretion defect of the
88 mutant Tg variants.

89 To address this shortcoming, we developed time-resolved interactome profiling
90 (TRIP) to capture and quantify interactions between Tg and interacting partners
91 throughout the life cycle of the protein. We found that Tg mutants are characterized by
92 both discrete changes with select PN components and broad temporal alterations
93 across Hsp70/90 and disulfide/redox processing pathways. Moreover, we find that these
94 perturbations are correlated with alterations in interactions with degradation compo-
95 nents. We coupled our TRIP method with functional siRNA screening and uncovered

96 that VCP and TEX264 are two key regulators of Tg processing. VCP and TEX264 inhi-
97 bition or silencing in thyroid cells resulted in rescued secretion of mutant Tg, represent-
98 ing – to our knowledge – the first restorative approach based upon proteostasis modula-
99 tion to increase mutant Tg secretion.
100
101 **RESULTS**
102
103 **TRIP temporally resolves Tg interactions with PQC components**
104 To develop the time-resolved interactome profiling method, we envisioned a two-stage
105 enrichment strategy utilizing pulsed biorthogonal unnatural amino acid labeling and
106 functionalization. After pulse labeling with homopropargylglycine (Hpg), samples can be
107 collected across time points throughout the chase period (Beatty et al., 2006; Kiick et
108 al., 2001). After conjugating the Hpg alkyne using copper-catalyzed alkyne-azide cy-
109 cloaddition (CuAAC) the client protein of interest is globally captured and enriched using
110 immunoprecipitation. The second enrichment step can then utilize a biotin-streptavidin
111 pulldown to capture the pulsed, Hpg-labeled, and CuAAC conjugated population, en-
112 riching samples into time-resolved fractions for quantitative liquid chromatography – tan-
113 dem mass spectrometry (LC-MS/MS) analysis with tandem mass tag (TMTpro) multi-
114 plexing (Figure 1A) (Li et al., 2020; Thompson et al., 2019).
115 Thyroglobulin was chosen as model secretory client protein, and we generated
116 isogenic Fisher rat thyroid cells (FRT) cells that stably expressed WT Tg or mutant vari-
117 ants (A2234D and C1264R) (Figures S1A and S1B; Table S1). WT Tg is readily

118 secreted from the FRT cells while the C1264R Tg shows only minimal residual secretion
119 (~2% of WT when detected after immunoprecipitation) and A2234D is fully secretion de-
120 ficient, consistent with prior characterization of these variants (Figures S1B-S1D) (Hishi-
121 numa et al., 1999; Pardo et al., 2009). We first set out to determine if Tg could tolerate
122 immunoprecipitation after pulse Hpg labeling, dithiobis(succinimidyl propionate) (DSP)
123 crosslinking, and CuAAC conjugation with a trifunctional tetramethylrhodamine
124 (TAMRA)-Azide-Polyethylene Glycol (PEG)-Desthiobiotin probe. We showed previously
125 that a C-terminal FLAG-tag is tolerated by Tg and allows efficient immunoprecipitation,
126 while DSP crosslinker aids in capturing transient protein-protein interactions that take
127 place during Tg processing (Wright et al., 2021). We pulse-labeled FRT cells expressing
128 WT Tg for 4 hours with Hpg, performed DSP crosslinking, CuAAC, and tested our two-
129 stage enrichment strategy via western blot analysis (Figure 1A). The additional steps
130 did not significantly affect immunoprecipitation efficiency and allowed for robust purifica-
131 tion of WT Tg and well validated interacting proteins (Figure 1A, Box 1-Box 3; Figure 1B
132 and 1C). We benchmarked our TRIP approach by monitoring Tg interactors HSPA5,
133 HSP90B1, and PDIA4 (Baryshev et al.; Menon et al., 2007; Wright et al., 2021). Moreo-
134 ver, DSP crosslinking was necessary to capture these interactions after the dual purifi-
135 cation and stringent wash steps (Figure 1A, Box 4; Figure 1D).

136 Next, we investigated whether TRIP could temporally resolve interactions with
137 these PN components. We pulse labeled WT Tg FRT cells with Hpg for 1 hr, followed
138 by a 3 hr chase in regular media capturing time points in 30-minute intervals and ana-
139 lyzing via western blot (Figure 2A). For WT Tg, interactions with HSPA5 peaked within

140 the first 30 minutes of the chase period and rapidly declined, in line with previous obser-
141 vations, but PDIA4 interactions were not detectable by western blot analysis (Figure 2B)
142 (Kim and Arvan, 1995; Menon et al., 2007). To test the ability of TRIP to distinguish
143 temporal differences in PQC interactions across mutant Tg variants, we performed TRIP
144 on FRT cells expressing C1264R Tg, a known patient mutation implicated in CH (Hishi-
145 numa et al., 1999; Kanou et al., 2007). For C1264R, interactions with HSPA5 were
146 highly abundant at the 0 hr time point, peaked later in the chase period at 2 hours, and
147 then rapidly declined. A similar temporal profile was also observed for HSP90B1. Addi-
148 tionally, interactions with PDIA4 were detectable for C1264R and were found to gradu-
149 ally increase throughout the first 1.5 hours of the chase period, before rapidly declining
150 (Figure 2C). We noticed similar temporal profiles for HSPA5 and PDIA4 to our western
151 blot analysis, when measured via TMTpro LC-MS/MS as further outlined below (Figure
152 2D and 2E).
153 These data highlight the utility of TRIP to not only identify changes in protein in-
154 teractions over time but monitor how these interactions differ for a given protein of inter-
155 est across disease states. Moreover, these data corroborate our previous findings that
156 steady-state interactions with HSPA5, HSP90B1 and PDIA4 are elevated for C1264R
157 Tg. (Wright et al., 2021).
158
159 **TRIP identifies altered temporal dynamics associated with Tg processing**
160 We benchmarked the utility of our TRIP approach to temporally resolve previously iden-
161 tified and novel interactors, as the Tg interactome has not been fully characterized in

162 native tissue. TRIP was carried out in FRT cells stably expressing WT, A2234D, and
163 C1264R Tg. We focused on A2234D and C1264R Tg as they present with distinct de-
164 fects in Tg processing and mutations are localized in structurally distinct domains (Hishi-
165 numa et al., 1999; Kanou et al., 2007). Following the Hpg pulse-chase labeling scheme
166 and dual affinity purification, the time-resolved Tg fractions were trypsin/Lys-C digested
167 and labeled individually with isobaric TMTpro tags. Subsequently, two biological repli-
168 cate TRIP time courses (0, 0.5, 1, 1.5, 2, and 3 hr) could be pooled into a 16plex
169 TMTpro sample that was analyzed by LC-MS/MS (Figures 2A and 3A).
170 Aside from the experimental samples, we utilized a (–) biotin pulldown booster
171 (or carrier) channel with cells that were pulse-labeled with Hpg, underwent CuAAC func-
172 tionalization, and immunoprecipitation, but did not undergo biotin-streptavidin enrich-
173 ment. This booster sample acted to 1) aid in increased peptide/protein identification -
174 compared to the much lower abundant chase samples; and 2) benchmark Tg interac-
175 tors in FRT cells compared to our previously published dataset (Figure 3A) (Petelski et
176 al., 2021; Tsai et al., 2020). When comparing the booster channel to our (–)Hpg nega-
177 tive control samples, most previously identified Tg interactors were strongly and signifi-
178 cantly enriched (Figure S2; Table S2). Our dataset in this study showed appreciable
179 overlap between our previous results in HEK293T cells identifying 75 of the previous
180 171 Tg interactors, and identifying 198 new interactors (Figure 3B). We noticed several
181 ribosomal and proteasomal subunits, trafficking factors, and lysosomal components that
182 were not identified in our previous dataset (Figure S2; Table S2). We then took our list
183 of previously identified interactors and PQC components found to be enriched in the (–)

184 biotin pulldown samples compared to (–) Hpg and carried these proteins forward to
185 time-resolved analysis utilizing the Hpg-chase samples.

186 To map the time-resolved Tg PN interactome changes, we considered the Hpg
187 chase samples (0 – 3 hr) and compared the enrichment of Tg interactors to the (–) Hpg
188 control. The enrichments were normalized to Tg protein levels to account for gradual
189 changes due to Tg secretion or degradation (Figure 2B). We organized the interactors
190 according to distinct PN pathways known to influence Tg processing (Figures S3 and
191 S4; Tables S3-S5). We found that both A2234D and C1264R exhibited prolonged inter-
192 actions with components across Hsp70/90 and disulfide/redox processing pathways
193 (Figures 3C and 3D; Figure S4). Particularly, A2234D and C1264R showed increased
194 interactions with HSPA5, HSP90B1, HYOU1, DNAJC3, and SDF2L1 throughout the
195 chase period (Figure 3D). Conversely, WT interactions peaked at the 0 hr time point
196 and consistently tapered off for many of these components, with DNAJC3 and SDF2L1
197 mainly being enriched at the 0 hr time point (Figure 3D; Figures S3 and S4). We even
198 noticed altered temporal interactions for previously unidentified components including
199 EMC1 and EMC4 of the ER membrane complex (EMC) and CCDC47 of the PAT com-
200 plex, all of which are involved membrane protein processing within the ER (Figures 3E;
201 Figure S4) (Chitwood and Hegde, 2020; McGilvray et al., 2020a; Shurtleff et al., 2018).
202 WT Tg interactions with both CCDC47 and EMC1 peak at the end of the chase period,
203 yet for C1264R this temporal profile is inversed peaking at the 0 hr time point and slowly
204 tapering off. Nonetheless, it remains unclear why EMC and PAT complex components
205 might engage with luminal Tg during biosynthesis and folding.

206 Similar divergent temporal interactions were observed in the case of disulfide/re-
207 dox processing components. PDIA3, PDIA4, PDIA6, and ERP29 have all been heavily
208 implicated in Tg processing (Baryshev et al., 2006; di Jeso et al., 2005, 2014; Menon et
209 al., 2007). While WT interactions with these components showed similar trends as
210 Hsp70/90 chaperoning components, peaking at the 0 hr time point and consistently de-
211 creasing, prolonged mutant interactions peaked only at 1-1.5 hr time points for both
212 A2234D and C1264R (Figure 3F and 3G). Tg engages with several prolyl isomerization
213 and hydroxylation enzymes, although previous differences between mutant and WT in-
214 teractions were quite small and disparate across constructs (Wright et al., 2021). With
215 the utilization of TRIP, we discovered that previously identified interactors such as NID1,
216 P4HA1, and SERPINH1 show distinct patterns of altered temporal profiles from mutant
217 to WT Tg (Figure 3H).
218
219 **TRIP defines link between glycan processing and ER-phagy pathways.**
220 One area of particular interest was the crosstalk and correlation between interac-
221 tions with glycan processing components and degradation pathways. The link between
222 the glycosylation state of ER clients and ER-associated degradation (ERAD) is well es-
223 tablished, whereas more recently defined autophagy at the ER (ER-phagy) or ER to ly-
224 sosome-associated degradation (ERLAD) represent alternative degradation mecha-
225 nisms for ER clients (Chiritoiu et al., 2020; Christianson et al., 2008, 2012; Fregno et al.,
226 2018, 2021). Previously, we showed that A2234D and C1264R differ in interactions with
227 N glycosylation components, particularly the oligosaccharyltransferase (OST) complex.

228 Efficient A2234D degradation required both STT3A and STT3B isoforms of the OST,
229 which mediate co-translational or post-translational N-glycosylation, respectively. TRIP
230 revealed differential interactions with glycosylation components that may lead to altered
231 degradation dynamics. Many glycan processing enzymes, lectin chaperones, and sev-
232 eral subunits of the OST complex, including STT3A and STT3B were identified (Figure
233 3I, Figure S4). While STT3A interactions across all constructs showed similar temporal
234 profiles, we observed prolonged interactions for lectin chaperones CALR, CANX with
235 mutant Tg. The most striking difference observed was with the “gatekeeping” glycosyl-
236 transferase UGGT1. This protein regulates glycoprotein engagement and folding
237 through the CANX/CALR cycle by re-glycosylating ER clients, and thus triggering reen-
238 gagement with the lectin chaperone cycle (Lamriben et al., 2016). UGGT1 interactions
239 with WT remain moderate from 0.5-1.5 hrs and peak at 3 hrs, while interactions for
240 A2234D and C1264R peaked earlier and were more pronounced throughout the chase
241 period. These differential interactions with UGGT1 may suggest changes in monitoring
242 of the Tg folded state. Moreover, CANX has been directly linked to emerging mecha-
243 nisms of ERLAD for glycosylated ER clients (Forrester et al., 2019; Fregno et al., 2018).
244 Proteasomal and autophagic degradation pathways exhibited widely different in-
245 teractions dynamics for WT and mutant Tg (Figure 3J-3L). The ERAD associated lectin
246 OS9, and ATPase VCP/p97 both peaked at the 3 hr chase time point for WT Tg (Figure
247 3K). Conversely, A2234D exhibited early VCP interactions that decreased throughout
248 the chase, with OS9 interactions peaking at the 2 hr time point. For C1264R, we ob-
249 served much stronger and prolonged VCP interactions, as well as additional interactions

250 with the ERAD associated mannosidase EDEM3 and E3 ubiquitin ligase adaptor SEL1L
251 (Christianson et al., 2008, 2012) (Figure 3K).
252 Our original dataset identified several lysosomal components, yet it was unclear
253 how Tg might be delivered to the lysosome. Recent work has identified several selective
254 ER-phagy receptors, and highlighted ER-phagy mechanisms for the clearance of mu-
255 tant prohormones and other destabilized clients from the ER (Chen et al., 2021; Cun-
256 ningham et al., 2019). It was intriguing then to identify several lysosomal and autophagy
257 related components and observe differential temporal profiles across Tg constructs (Fig-
258 ure 3L, Figure S4). Both WT and C1264R Tg showed appreciable interactions with lyso-
259 somal components, while A2234D interactions with these components were more
260 sparse. Interactions with several lysosomal cathepsin proteases and glycan trimming
261 enzymes exhibited altered temporal profiles from WT to C1264R. We found that interac-
262 tions with these components peaked for WT at 1 hr, while C1264R interactions peaked
263 earlier and remained more stable throughout the chase period (Figure 3L and S4). Yet,
264 the most intriguing observation was the enrichment of three different ER-phagy recep-
265 tors, ATL3, CCPG1, and RTN3 between WT and C1264R, along with the RTN3 adaptor
266 protein PGRMC1 (Chen et al., 2019, 2021; Grumati et al., 2017; Liang et al., 2018;
267 Smith et al., 2018). ATL3 showed similar interaction patterns between WT and C1264R
268 with interactions rising and peaking at 1-1.5 hr time points before beginning to taper off.
269 On the other hand, CCPG1 and RTN3 were found to specifically interact with C1264R,
270 with RTN3 interactions peaking at 0 hr and then decreasing, while CCPG1 interactions
271 remained more stable (Figure 3L). Another striking observation was that the temporal

272 profile of EMC interactions for C1264R correlated with RTN3, PGRMC1, CTSB, and
273 CTSD interactions (Figure 3E and 3L). This is particularly interesting as there are few
274 known adaptor or accessory proteins that aid in client specific ER-phagy or ERLAD.
275 Overall, these data display the ability of our TRIP workflow to assess the tem-
276 poral dynamics associated with PQC, providing further insight into the dysregulation of
277 interactions within CH dyshormonogenesis. It is worth noting that many interactors, in-
278 cluding CANX, ERP29, and VCP amongst others, previously did not show any apprecia-
279 ble changes in interactions from WT to mutant Tg when using traditional AP-MS meth-
280 ods, yet TRIP was able to identify and highlight these unseen changes over time
281 (Wright et al., 2021).
282
283 **siRNA screening discovers key regulators of construct specific Tg processing**
284 To investigate and better comprehend the functional implications of Tg interactors and
285 other PQC components we developed an RNA interference screening platform. Moreo-
286 ver, we hoped to identify factors whose modulation may act to rescue mutant Tg secre-
287 tion. HEK293 cells were engineered to stably express nanoluciferase-tagged Tg con-
288 structs (Tg-NLuc) and screened against 167 Tg interactors and related PN components.
289 The NLuc tag allowed us to monitor changes to both intracellular Tg abundance in the
290 cell lysates, and Tg levels in the conditioned media to assess secretion rates in a 96-
291 well format. Importantly, the NLuc-tag did not alter the secretion of WT Tg, and CH-as-
292 sociated mutants maintained the same secretion deficiency (Figure 4A, Figures S1E-
293 S1K) (England et al., 2016). We identified 4 genes whose silencing modulated Tg-NLuc

294 abundance in lysate (Figures 4B, Figure S5A; Table S6). Silencing of NAPA (α-SNAP)
295 and LMAN1 were found to increase WT Tg-NLuc lysate abundance but had no effects
296 on the two mutants. α-SNAP is a member of the Soluble N-ethylmaleimide-sensitive
297 factor Attachment Protein (SNAP) family and plays a critical role in vesicle fusion and
298 docking, while LMAN1 is a mannose-specific lectin that functions as a glycoprotein
299 cargo receptor for ER-to-Golgi trafficking (Marinko et al., 2021; Song et al., 2017; Zhao
300 et al., 2007). For mutant Tg-NLuc constructs we found cathepsin Z (CTSZ) silencing de-
301 creased A2234D Tg-NLuc lysate abundance, while β-glucoronidase (GUSB) silencing
302 increased C1264R lysate abundance (Figure 4B, Figure S5A; Table S6).
303 When monitoring secreted Tg-NLuc levels in the conditioned media, we identified
304 8 genes whose silencing led to differential changes in Tg-NLuc secretion (Figures 4C,
305 Figure S5B; Table S6). α-SNAP, neuraminidase 1 (NEU1), and nodal modulator 2
306 (NOMO2) silencing led to decreases in Tg-NLuc secretion, with α-SNAP & NEU1 affect-
307 ing WT, and NOMO2 affecting A2234D in a construct specific manner. The decrease in
308 WT Tg secretion upon α-SNAP silencing complemented the results of increased WT ly-
309 sate levels, indicating a shift from secretion towards retention. NEU1 is a lysosomal en-
310 zyme that cleaves terminal sialic acid residues on proteins and lipid species
311 (Pshezhetsky and Hinek, 2011; Ryuzono et al., 2016). While Tg contains terminal sialic
312 residues after glycan maturation through the Golgi complex, it is unclear how silencing
313 of NEU1 might decrease secretion of WT Tg (Citterio et al., 2019). NOMO2 is one of
314 three close homologs of the NOMO gene believed to share similar functions, with
315 NOMO recently identified as a component of the TMCO1-ribosome complex/translocon

316 involved in membrane protein biogenesis and found to be a close interactor with ER-
317 phagy receptor TEX264 (An et al., 2019; McGilvray et al., 2020b).
318 Remarkably, we identified 6 genes whose silencing rescued mutant Tg-NLuc se-
319 cretion in a construct specific manner. α-SNAP silencing increased secretion of A2234D
320 Tg-NLuc. This contrast to the reduction in WT secretion may suggest an alternative role
321 for α-SNAP in regulating mutant Tg processing as other proteins involved in vesicular
322 fusion and trafficking have been implicated in ER-phagy (Cui et al., 2019; Liang et al.,
323 2020). Silencing of LEPRE1 (P3H1), an ER-resident prolyl hydroxylase, increased
324 C1264R Tg-NLuc secretion but not WT nor A2234D (Vranka et al., 2004). Silencing of
325 several protein degradation genes robustly increased mutant Tg secretion. VCP silenc-
326 ing increased both A2234D and C1264R Tg-NLuc secretion (Figure 4C, Figure S5B;
327 Table S6). As mentioned previously, VCP is associated with ERAD but also aids in sev-
328 eral diverse cellular functions including the interplay between proteasomal and lysoso-
329 mal degradation (Christianson et al., 2008, 2012; Hill et al., 2021). HERPUD1, TEX264
330 and RTN3 silencing selectively increased C1264R secretion, but did not alter WT nor
331 A2234D secretion. HERPUD1 is a ubiquitin-like protein and associates with VCP during
332 ERAD (Christianson et al., 2012; Needham et al., 2019; Okuda-Shimizu and Hender-
333 shot, 2007). The ER-phagy receptors RTN3 and TEX264 localize to sub domains of the
334 ER to facilitate degradation of specific ER clients and organellular regions (An et al.,
335 2019; Chen et al., 2021; Chino et al., 2019; Cunningham et al., 2019; Fielden et al.,
336 2022; Grumati et al., 2017). Of note, while the ER-phagy receptor CCPG1 was identified
337 in our mass spectrometry dataset siRNA silencing of CCPG1 did not significantly alter

338 Tg-NLuc abundance in lysate or media, nor did silencing of SEC62 or RETREG1
339 (FAM134B), two additional ER-phagy receptors found to regulate ER dynamics (Figure
340 S5; Table S6).
341 This is the first study to broadly investigate the functional implications of Tg in-
342 teractors and other PQC network components on Tg processing through siRNA screen-
343 ing. Particularly, with many of these components being involved in protein degradation
344 these results may suggest that the blockage of degradation pathways can broadly res-
345 cue the secretion of A2234D and C1264R mutant Tg, a phenomenon similarly found in
346 other protein folding diseases (Vij et al., 2006).
347
348 **Trafficking and degradation factors selectively regulate Tg processing in thyroid**
349 **cells**
350 We examined the hits from the siRNA screen in FRT cells stably expressing Tg con-
351 structs to test whether their silencing exhibited similar phenotypes in thyroid specific tis-
352 sue. First, WT Tg FRT cells were transfected with siRNAs targeting LMAN1 and NAPA
353 (α-SNAP), and changes in Tg lysate and media abundance were monitored. Silencing
354 of α-SNAP led to a ~50% increase in WT Tg lysate abundance, while α-SNAP and
355 LMAN1 silencing both led to marginal decreases in WT Tg secretion after 4 hrs, con-
356 sistent with the results in HEK293 cells (Figure 5A and 5B). ^{35}S pulse-chase analysis
357 also confirmed that α-SNAP silencing significantly increased lysate retention by 15%
358 and decreased secretion by 18% (Figure S7A and S7B).

359 Next, C1264R Tg FRT cells were transfected with siRNAs targeting VCP, RTN3,
360 TEX264, HERPUD1, and LEPRE1 (P3H1) and lysate and media Tg abundance were
361 similarly monitored. RTN3, TEX264, and HERPUD1 silencing marginally, yet signifi-
362 cantly decreased C1264R lysate abundance (Figure 5C and 5D). Moreover, VCP and
363 TEX264 silencing significantly increased C1264R secretion by 3-fold and 2-fold respec-
364 tively after 8 hrs, in line with our results in HEK293 cells (Figures 5C and 5D). In con-
365 trast, silencing of RTN3 significantly decreased C1264R Tg secretion by 5-fold, opposite
366 to the increased secretion observed in HEK293 cells. Efficient silencing of all proteosta-
367 sis factors in FRT cells was also confirmed (Figure S6).
368
369 **Mutant Tg is selectively enriched with the ER-phagy receptor TEX264**
370 Intrigued by the finding that TEX264 silencing increased C1264R Tg secretion without
371 affecting WT Tg, we asked whether TEX264 exhibited differential interactions with Tg
372 constructs. HEK293 Tg-NLuc cells were transfected with either a fluorescent GFP con-
373 trol, or C-terminal FLAG-tagged ER-phagy receptors SEC62 and TEX264 and FLAG co-
374 immunoprecipitations (co-IP) were performed. We then used the NLuc assay and West-
375 ern blotting to monitor Tg enrichment in the SEC62 or TEX264 co-IP (Figure 6A).
376 SEC62 silencing did not affect the processing of any Tg constructs in our siRNA screen
377 and therefore should act as a negative control (Figure S5; Table S6). We found that co-
378 IP of SEC62 did not yield any appreciable enrichment of Tg compared to GFP control.
379 Conversely, co-IP of TEX264 resulted in the enrichment of all Tg constructs compared
380 to GFP control when monitored by NLuc assay, with C1264R and A2234D being

381 significantly enriched. C1264R Tg exhibited a 3-fold increase in interactions compared
382 to WT Tg and almost a 2-fold increase compared to A2234D Tg (Figure 6B). This in-
383 crease in C1264R enrichment was also observable by western blot analysis (Figure
384 6C).

385 Together, these data suggest that not only does TEX264 play a role in Tg pro-
386 cessing, but CH-associated Tg mutants are selectively targeted to TEX264. Further-
387 more, ER-phagy should be considered a major degradative pathway in Tg processing,
388 as other studies have mainly focused on Tg degradation through ERAD (Menon et al.,
389 2007; Tokunaga et al., 2000).

390

391 **Pharmacological VCP Inhibition Selectively Rescues C1264R Tg Secretion**

392 Considering the exciting finding that silencing of degradation factors by siRNA rescued
393 C1264R secretion, we sought to investigate whether pharmacological modulation of se-
394 lect Tg processing components could similarly improve Tg secretion. There are no se-
395 lective inhibitors currently available for TEX264, but several for VCP. We monitored
396 C1264R Tg secretion from FRT cells in the presence of VCP inhibitors ML-240, CB-
397 5083, and NMS-873 and found treatment with ML-240 was able to significantly increase
398 C1264R Tg secretion, corroborating our siRNA silencing data (Figure 7A and 7B) (Chou
399 et al., 2013, 2014; Zhou et al., 2015). Further, VCP inhibition in FRT cells with ML-240
400 did not alter C1264R Tg lysate abundance. To investigate whether this rescue of
401 C1264R Tg secretion with ML-240 treatment was specific to C1264R Tg, we also moni-
402 tored WT Tg abundance. In contrast, we observed that ML-240 significantly reduced

403 WT Tg abundance in both lysate and media 4 and 8 hrs after treatments (Figures 7C
404 and 7D).

405 We hypothesized that ML-240 treatment may differentially regulate Tg degrada-
406 tion and processing in a construct specific manner. We turned to a ^{35}S pulse-chase as-
407 say to fully characterize Tg degradation and processing dynamics with ML-240 treat-
408 ment and found that lysate abundance of C1264R Tg was not significantly changed at
409 the 4 hr time point with ML-240 treatment compared to DMSO (Figure 7E; Figure S7C
410 and S7D). This paralleled the previous results with VCP silencing, and ML-240 treat-
411 ment under steady-state conditions in FRT cells. Excitingly, we found a 10-fold increase
412 in C1264R Tg secretion at the 4 hr time point with ML-240 treatment compared to
413 DMSO with no significant change in C1264R Tg degradation in the presence of ML-240
414 (Figure 7E, Figure S7D). Conversely, for WT Tg ML-240 treatment led to a significant
415 increase in lysate accumulation at 4 hrs compared to DMSO (Figure 7F; Figure S7E
416 and S7F). This increase in lysate abundance correlated with a significant decrease in
417 WT Tg secretion from 67% to 4% in the presence of ML-240 compared to DMSO, with-
418 out altering WT degradation (Figure S7F).

419

420 **Pharmacological VCP Inhibition is Associated with Temporal Remodeling of the**
421 **Tg Interactome**

422 We were curious if our TRIP method was capable of capturing changes in interactions
423 across PQC pathways that mediate the rescued secretion of C1264R Tg. Hence, TRIP
424 of C1264R Tg was carried out in the presence of ML-240 to monitor temporal changes

425 across key PQC pathways (Figures S8A-S8C; Tables S4 and S5). Both glycan pro-
426 cessing and Hsp70/90 chaperoning pathways exhibited broad decreases in C1264R Tg
427 interactions in ML-240 treated samples compared to the untreated controls (Figure 7G
428 and 7H). Particularly, CANX and UGGT1 interactions tapered off more rapidly within 0.5
429 hr compared to untreated C1264R. In contrast, interactions with key Hsp70/90 chaper-
430 ones components remained relatively steady throughout the chase period before peak-
431 ing at the 3 hr time point (Figure 7I and 7J). Conversely, C1264R interactions with co-
432 chaperones DNAJB11 and DNAJC10 decreased and mimicked the WT Tg temporal
433 profile (Figure 3D and 7J).
434 Interactions with disulfide/redox processing and prolyl isomerization and hydrox-
435 ylation components exhibited milder but marked declines at intermediate time points
436 with ML-240 treatment compared to untreated samples (Figure 7K and 7L; Figure S8C).
437 PDIA6 and TXNDC12 interactions peaked at the 0 hr time point and tapered off
438 throughout the chase period, while PDIA4 interactions remained relatively low before
439 peaking at the 3 hr time point (Figure 7L). Conversely, ERP29 and PDIA3 interactions
440 remained largely unchanged in the presence of ML-240. These more drastic changes in
441 glycan processing and Hsp70/90 chaperone interactions may highlight that extensive
442 early interactome remodeling during N-glycosylation and Hsp70/90 dependent folding
443 could be a key rescue mechanism. Conversely, remodeling with disulfide/redox pro-
444 cessing components during secretion rescue of C1264R involves more discrete
445 changes in interactions, and prolyl isomerization and hydroxylation likely play a minor
446 role during this secretion rescue.

447 We monitored the activation of UPR markers in the presence of ML-240 and
448 found that 3 hr treatment with ML-240 left HSPA5 and ASNS expression unchanged in
449 C1264R Tg cells but led to a significant decrease in WT Tg cells. Only DNAJB9 tran-
450 scripts showed a small, but significant increase in both WT Tg and C2164R Tg FRT
451 cells (Figure S8D). Moreover, ML-240 did not significantly alter cell viability after 3
452 hours, as measured by propidium iodide staining (Figure S8E-S8G). Overall, these re-
453 sults suggest that ML-240 can selectively rescue C1264R Tg secretion, and that this
454 rescue is correlated with unique temporal changes in C1264R Tg PN interactions, but
455 not global remodeling of the ER proteostasis network due to UPR activation.
456

457 **DISCUSSION**

458 The timing of protein-protein interactions implicated in cellular processes and patho-
459 genic states remains pivotal to our understanding of disease mechanisms. Nonetheless,
460 the temporal measurement of protein-protein interactions has remained difficult and
461 proven to be a bottleneck in elucidating the coordination of complex biological pathways
462 such as the proteostasis network. Here, we have presented an approach utilizing a two-
463 stage enrichment strategy to temporally resolve protein-protein interactions implicated in
464 PQC. Furthermore, we utilized a functional genomic screen to further characterize and
465 investigate the implications of these protein-protein interactions on Tg processing. This
466 combination of our novel TRIP approach coupled with functional screening deconvo-
467 luted previously established PQC mechanisms for Tg processing while also providing
468 new paradigms within PQC pathways that are critical for secretion of the prohormone.

469 TRIP has allowed identification and resolution of unique temporal changes in Tg
470 interactions with glycan processing components including STT3B, CANX, CALR, and
471 UGGT1, while contrasting WT to mutant Tg variants. These changes subsequently cor-
472 relate with altered interactions with ERAD components EDEM3, OS9, SEL1L, and VCP.
473 Moreover, we identified a broader scope of Tg interactors in thyroid tissue, including
474 ER-phagy receptors ATL3, CCPG1, RTN3, and the RTN3 adaptor protein PGRMC1.
475 Identification of these receptors establishes a direct link from Tg processing to ER-
476 phagy or ERLAD degradation mechanisms. Additionally, glycan dependent and inde-
477 pendent mechanisms have been established for the degradation of ERAD resistant ER
478 clients (Fregno et al., 2021; He et al., 2021). This overlap in degradation pathways may
479 be similarly at play in the case of Tg biogenesis and processing, especially for mutants
480 forming difficult to degrade aggregates (di Jeso et al., 2005, 2014; Kim et al., 1993;
481 Menon et al., 2007).
482 An important finding was that TRIP was capable of resolving subtle temporal in-
483 teraction changes, for example with CANX, ERP29, and VCP, which were otherwise
484 masked in steady-state interactomics data. Nonetheless, there are some limitations
485 within our TRIP methodology. TRIP relies on a two-stage purification strategy which in-
486 creases sample handling and limits the amount of protein that can be subsequently en-
487 riched. Both add inherent variability to the workflow. Furthermore, pulsed labeling with
488 unnatural amino acids has been shown to slow portions of protein translation (Bagert et
489 al., 2014; Dieterich et al., 2006; Kiick et al., 2001; Lang and Chin, 2014). Additionally,
490 within our dataset we noticed that the temporal profiles for ribosomal and proteasomal

491 subunits, trafficking and lysosomal components are inherently difficult to measure
492 across experiments. To efficiently measure these components temporally the TRIP
493 methodology will require further optimization.

494 The functional implications of protein-protein interactions can be difficult to de-
495 duce, especially in the case of PQC mechanisms containing several layers of redun-
496 dancy across stress response pathways, paralogs, and multiple unique proteins sharing
497 similar functions (Bludau and Aebersold, 2020; Braakman and Hebert, 2013; Karagöz et
498 al., 2019; Wright and Plate, 2021). This led us to establish a siRNA screening platform
499 to broadly investigate the functional implications of PQC components to complement
500 our TRIP data. With this assay we found the trafficking factor NAPA (α-SNAP) was
501 heavily implicated in WT Tg secretion. Most strikingly, we found that VCP and TEX264
502 were implicated in C1264R processing, and siRNA silencing of either led to rescue of
503 C1264R secretion. Rescue of mutant Tg trafficking from ER to Golgi, but not secretion,
504 with low-temperature correction had been documented previously (Kim et al., 1996).Yet,
505 this is the first study, to our knowledge, that identified a restorative approach to mutant
506 Tg secretion. To expound upon this, our findings that pharmacological VCP inhibition
507 selectively rescues C1264R secretion compared to WT, and mutant Tg was selectively
508 enriched with TEX264 further corroborated the TRIP data establishing that Tg mutants
509 undergo differential interactions with degradation pathways compared to WT Tg. Similar
510 phenomena have been observed for the partitioning and differential interactions of other
511 prohormone proteins, such as proinsulin and proopiomelanocortin, and proteasome re-
512 sistant polymers of alpha1-antitrypsin Z-variant. RTN3 is implicated in these differential

513 interactions and is shown to be selective for these prohormones compared to other ER-
514 phagy receptors (Chen et al., 2021; Cunningham et al., 2019; Fregno et al., 2018).
515 While A2234D and C1264R Tg were preferentially enriched with TEX264 compared to
516 WT, it remains unclear what other accessory proteins may be necessary for the recogni-
517 tion of TEX264 clients (An et al., 2019; Chino et al., 2019). Furthermore, TEX264 func-
518 tion in both protein degradation and DNA damage repair further complicates RNAi
519 based investigations (Fielden et al., 2022). Finally, as we discovered that pharmacolog-
520 ical VCP inhibition can rescue C1264R secretion yet is detrimental for WT processing, it
521 is unclear whether VCP may exhibit distinct functions for WT and mutant Tg PQC.
522 We used our TRIP method to monitor the changes in interactions associated with
523 the rescue of C1264R with pharmacological VCP inhibition. We found that this rescue is
524 correlated with broad temporal changes in interactions across both glycan processing
525 and Hsp70/90 chaperone pathways, while exhibiting more discrete changes with select
526 disulfide/redox processing components and leaving interactions with prolyl isomerization
527 and hydroxylation components largely unchanged. Mapping these temporal changes in
528 response to pharmacological VCP inhibition and C1264R rescue highlights the capabili-
529 ties of TRIP to not only resolve protein-protein interactions across disease states but
530 also identify compensatory mechanisms that may take place with drug treatment or
531 other modulating techniques like gene inhibition or activation that can correct or modu-
532 late disease states. Consequently, TRIP may find broad applicability for delineating the
533 proteostasis deficiencies that give rise to diverse protein misfolding diseases and eluci-
534 dating other cellular interactome dynamics.

535

536 **STAR*METHODS**

537 Detailed methods are provided in the online version of this paper and included the fol-

538 lowing

539 - KEY RESOURCES TABLE
540 - LEAD CONTACT AND METERIALS AVAILABILITY
541 - METHOD DETAILS
542 - Plasmid Production and Antibodies
543 - Cell Line Engineering
544 - Time-Resolved Interactome Profiling
545 - Liquid Chromatography – Tandem Mass Spectrometry
546 - Immunoblotting and SDS-PAGE
547 - qRT-PCR
548 - siRNA Screening Assay
549 - FRT siRNA Validation Studies
550 - 35 S Pulse Chase Assay
551 - VCP Pharmacological Inhibition Studies
552 - TEX264 & Tg-NLuc Co-Immunoprecipitation Studies
553 - QUANTIFICATION AND STATISTICAL ANALYSIS
554 - Mass Spectrometry Interactomics and TMT Quantification
555 - DATA AND CODE AVAILABILITY

556

SUPPLEMENTAL INFORMATION

Supplemental Information can be found online at #####

ACKNOWLEDGEMENTS

M.T.W. was supported by the National Science Foundation – Graduate Research Fellowship Program. This work was also funded by an NIGMS R35 award (1R35GM133552). This content is solely the responsibility of the authors and does not necessarily represent the official views of the National Institutes of Health.

AUTHOR CONTRIBUTIONS

M.T.W. and L.P. designed experiments. All authors performed experiments. M.T.W. and L.P. wrote the manuscript. All authors contributed feedback for the manuscript.

DECLARATION OF INTEREST

The authors declare no competing interests.

REFERENCES

An, H., Ordureau, A., Paulo, J.A., Shoemaker, C.J., Denic, V., and Harper, J.W. (2019). TEX264 Is an Endoplasmic Reticulum-Resident ATG8-Interacting Protein Critical for ER Remodeling during Nutrient Stress. Mol Cell *74*, 891-908.e10. https://doi.org/10.1016/j.molcel.2019.03.034 PMID - 31006537.

Bagert, J.D., Xie, Y.J., Sweredoski, M.J., Qi, Y., Hess, S., Schuman, E.M., and Tirrell, D.A. (2014). Quantitative, Time-Resolved Proteomic Analysis by Combining Bioorthogonal Noncanonical Amino Acid Tagging and Pulsed Stable Isotope Labeling by Amino Acids in Cell Culture. Molecular & Cellular Proteomics *13*, 1352–1358. https://doi.org/10.1074/mcp.m113.031914 PMID - 24563536.

Baryshev, M., Sargsyan, E., and Mkrtchian, S. (2006). ERp29 is an essential endoplasmic reticulum factor regulating secretion of thyroglobulin. Biochem Biophys Res Commun *340*, 617–624. https://doi.org/10.1016/j.bbrc.2005.12.052.

Baryshev, M., Sargsyan, E., Wallin, G., Lejnieks, A., Furudate, S., Hishinuma, A., and Mkrtchian, S. Unfolded protein response is involved in the pathology of human congenital hypothyroid goiter and rat non-goitrous congenital hypothyroidism. J Mol Endocrinol *32*, 903 920. https://doi.org/10.1677/jme.0.0320903 PMID - 15171721.

Beatty, K.E., Liu, J.C., Xie, F., Dieterich, D.C., Schuman, E.M., Wang, Q., and Tirrell, D.A. (2006). Fluorescence Visualization of Newly Synthesized Proteins in Mammalian Cells. Angewandte Chemie International Edition *45*, 7364–7367. https://doi.org/10.1002/ANIE.200602114.

Behnke, J., Mann, M.J., Scruggs, F.-L., Feige, M.J., and Hendershot, L.M. (2016). Members of the Hsp70 Family Recognize Distinct Types of Sequences to Execute ER Quality Control. Mol Cell *63*, 739 752. https://doi.org/10.1016/j.molcel.2016.07.012 PMID - 27546788.

van Bergen, W., Heck, A.J.R., and Baggelaar, M.P. (2021). Recent advancements in mass spectrometry–based tools to investigate newly synthesized proteins. Curr Opin Chem Biol *66*. https://doi.org/10.1016/J.CBPA.2021.07.001.

Bludau, I., and Aebersold, R. (2020). Proteomic and interactomic insights into the molecular basis of cell functional diversity. Nat Rev Mol Cell Biol *21*, 327–340. https://doi.org/10.1038/s41580-020-0231-2.

Braakman, I., and Hebert, D.N. (2013). Protein Folding in the Endoplasmic Reticulum. Cold Spring Harb Perspect Biol *5*, a013201–a013201. https://doi.org/10.1101/cshperspect.a013201.

Chen, E.Y., Tan, C.M., Kou, Y., Duan, Q., Wang, Z., Meirelles, G. v., Clark, N.R., Ma'ayan, A., and Ma'ayan, A. (2013). Enrichr: interactive and collaborative HTML5 gene list enrichment analysis tool. BMC Bioinformatics *14*, 128. https://doi.org/10.1186/1471-2105-14-128.

Chen, Q., Xiao, Y., Chai, P., Zheng, P., Teng, J., and Chen, J. (2019). ATL3 Is a Tubular ER-Phagy Receptor for GABARAP-Mediated Selective Autophagy. Curr Biol *29*, 846-855.e6. https://doi.org/10.1016/j.cub.2019.01.041.

619 Chen, Y.J., Knupp, J., Arunagiri, A., Haataja, L., Arvan, P., and Tsai, B. (2021).
620 PGRMC1 acts as a size-selective cargo receptor to drive ER-phagic clearance of mu-
621 tant prohormones. Nat Commun *12*. https://doi.org/10.1038/S41467-021-26225-8.

622 Chino, H., Hatta, T., Natsume, T., and Mizushima, N. (2019). Intrinsically Disordered
623 Protein TEX264 Mediates ER-phagy. Mol Cell *74*, 909-921.e6.
624 https://doi.org/10.1016/j.molcel.2019.03.033 PMID - 31006538.

625 Chiritoiu, M., Chiritoiu, G.N., Munteanu, C.V.A., Pastrama, F., Erwin Ivessa, N., and
626 Petrescu, S.M. (2020). EDEM1 Drives Misfolded Protein Degradation via ERAD and Ex-
627 ploits ER-Phagy as Back-Up Mechanism When ERAD Is Impaired. Int J Mol Sci *21*.
628 https://doi.org/10.3390/IJMS21103468.

629 Chitwood, P.J., and Hegde, R.S. (2020). An intramembrane chaperone complex facili-
630 tates membrane protein biogenesis. Nature *584*, 630–634.
631 https://doi.org/10.1038/s41586-020-2624-y.

632 Chou, T.F., Li, K., Frankowski, K.J., Schoenen, F.J., and Deshaies, R.J. (2013). Struc-
633 ture–Activity Relationship Study Reveals ML240 and ML241 as Potent and Selective In-
634 hibitors of p97 ATPase. ChemMedChem *8*, 297–312.
635 https://doi.org/10.1002/CMDC.201200520.

636 Chou, T.F., Bulfer, S.L., Weihl, C.C., Li, K., Lis, L.G., Walters, M.A., Schoenen, F.J., Lin,
637 H.J., Deshaies, R.J., and Arkin, M.R. (2014). Specific Inhibition of p97/VCP ATPase and
638 Kinetic Analysis Demonstrate Interaction between D1 and D2 ATPase Domains. J Mol
639 Biol *426*, 2886–2899. https://doi.org/10.1016/J.JMB.2014.05.022.

640 Christianson, J.C., Shaler, T.A., Tyler, R.E., and Kopito, R.R. (2008). OS-9 and GRP94
641 deliver mutant α1-antitrypsin to the Hrd1–SEL1L ubiquitin ligase complex for ERAD. Nat
642 Cell Biol *10*, 272–282. https://doi.org/10.1038/ncb1689 PMID - 18264092.

643 Christianson, J.C., Olzmann, J.A., Shaler, T.A., Sowa, M.E., Bennett, E.J., Richter,
644 C.M., Tyler, R.E., Greenblatt, E.J., Harper, J.W., and Kopito, R.R. (2012). Defining hu-
645 man ERAD networks through an integrative mapping strategy. Nat Cell Biol *14*, 93–105.
646 https://doi.org/10.1038/ncb2383 PMID - 22119785.

647 Chung, N., Zhang, X.D., Kreamer, A., Locco, L., Kuan, P.-F., Bartz, S., Linsley, P.S.,
648 Ferrer, M., and Strulovici, B. (2008). Median Absolute Deviation to Improve Hit Selection
649 for Genome-Scale RNAi Screens. J Biomol Screen *13*, 149–158.
650 https://doi.org/10.1177/1087057107312035 PMID - 18216396.

651 Citterio, C.E., Targovnik, H.M., and Arvan, P. (2019). The role of thyroglobulin in thyroid
652 hormonogenesis. Nat Rev Endocrinol *15*, 323–338. https://doi.org/10.1038/s41574-019-
653 0184-8 PMID - 30886364.

654 Cortez, D. (2017). Proteomic Analyses of the Eukaryotic Replication Machinery. In
655 Methods in Enzymology, pp. 33–53.

656 Coscia, F., Taler-Verčič, A., Chang, V.T., Sinn, L., O'Reilly, F.J., Izoré, T., Renko, M.,
657 Berger, I., Rappsilber, J., Turk, D., et al. (2020). The structure of human thyroglobulin.
658 Nature *578*, 1–4. https://doi.org/10.1038/s41586-020-1995-4 PMID - 32025030.

Cui, Y., Parashar, S., Zahoor, M., Needham, P.G., Mari, M., Zhu, M., Chen, S., Ho, H.-C., Reggiori, F., Farhan, H., et al. (2019). A COPII subunit acts with an autophagy receptor to target endoplasmic reticulum for degradation. Science (1979) *365*, 53–60. https://doi.org/10.1126/science.aau9263.

Cunningham, C.N., Williams, J.M., Knupp, J., Arunagiri, A., Arvan, P., and Tsai, B. (2019). Cells Deploy a Two-Pronged Strategy to Rectify Misfolded Proinsulin Aggregates. Mol Cell *75*, 442-456.e4. https://doi.org/10.1016/J.MOLCEL.2019.05.011.

Dieterich, D.C., Link, A.J., Graumann, J., Tirrell, D.A., and Schuman, E.M. (2006). Selective identification of newly synthesized proteins in mammalian cells using bioorthogonal noncanonical amino acid tagging (BONCAT). Proceedings of the National Academy of Sciences *103*, 9482–9487. https://doi.org/10.1073/pnas.0601637103.

England, C.G., Ehlerding, E.B., and Cai, W. (2016). NanoLuc: A Small Luciferase Is Brightening Up the Field of Bioluminescence. Bioconjug Chem *27*, 1175–1187. https://doi.org/10.1021/acs.bioconjchem.6b00112 PMID - 27045664.

Fielden, J., Popović, M., and Ramadan, K. (2022). TEX264 at the intersection of autophagy and DNA repair. Autophagy *18*, 40. https://doi.org/10.1080/15548627.2021.1894059.

Fonslow, B.R., Niessen, S.M., Singh, M., Wong, C.C.L., Xu, T., Carvalho, P.C., Choi, J., Park, S.K., and Yates, J.R. (2012). Single-step inline hydroxyapatite enrichment facilitates identification and quantitation of phosphopeptides from mass-limited proteomes with MudPIT. J Proteome Res *11*, 2697–2709. https://doi.org/10.1021/PR300200X/SUPPL_FILE/PR300200X_SI_002.XLS.

Forrester, A., de Leonibus, C., Grumati, P., Fasana, E., Piemontese, M., Staiano, L., Fregno, I., Raimondi, A., Marazza, A., Bruno, G., et al. (2019). A selective ER-phagy exerts procollagen quality control via a Calnexin-FAM134B complex. EMBO J *38*. https://doi.org/10.15252/embj.201899847.

Fregno, I., Fasana, E., Bergmann, T.J., Raimondi, A., Loi, M., Soldà, T., Galli, C., D'Antuono, R., Morone, D., Danieli, A., et al. (2018). ER-to-lysosome-associated degradation of proteasome-resistant ATZ polymers occurs via receptor-mediated vesicular transport. EMBO J *37*. https://doi.org/10.15252/EMBJ.201899259.

Fregno, I., Fasana, E., Soldà, T., Galli, C., and Molinari, M. (2021). N-glycan processing selects ERAD-resistant misfolded proteins for ER-to-lysosome-associated degradation. EMBO J e107240. https://doi.org/10.15252/embj.2020107240 PMID - 34152647.

Grumati, P., Morozzi, G., Hölper, S., Mari, M., Harwardt, M.-L.I.E., Yan, R., Müller, S., Reggiori, F., Heilemann, M., and Dikic, I. (2017). Full length RTN3 regulates turnover of tubular endoplasmic reticulum via selective autophagy. Elife *6*, e25555. https://doi.org/10.7554/elife.25555 PMID - 28617241.

He, L., Kennedy, A.S., Houck, S., Aleksandrov, A., Quinney, N.L., Cyr-Scully, A., Cholon, D.M., Gentzsch, M., Randell, S.H., Ren, H.Y., et al. (2021). DNAJB12 and Hsp70

triage arrested intermediates of N1303K-CFTR for endoplasmic reticulum-associated autophagy. Mol Biol Cell *32*, 538–553. https://doi.org/10.1091/mbc.E20-11-0688.

Hill, S.M., Wrobel, L., Ashkenazi, A., Fernandez-Estevez, M., Tan, K., Bürli, R.W., and Rubinsztein, D.C. (2021). VCP/p97 regulates Beclin-1-dependent autophagy initiation. Nat Chem Biol *17*, 448–455. https://doi.org/10.1038/S41589-020-00726-X.

Hishinuma, A., Takamatsu, J., Ohyama, Y., Yokozawa, T., Kanno, Y., Kuma, K., Yoshida, S., Matsuura, N., and Ieiri, T. (1999). Two Novel Cysteine Substitutions (C1263R and C1995S) of Thyroglobulin Cause a Defect in Intracellular Transport of Thyroglobulin in Patients with Congenital Goiter and the Variant Type of Adenomatous Goiter1. J Clin Endocrinol Metab *84*, 1438–1444. https://doi.org/10.1210/jcem.84.4.5633.

Howden, A.J.M., Geoghegan, V., Katsch, K., Efstathiou, G., Bhushan, B., Boutureira, O., Thomas, B., Trudgian, D.C., Kessler, B.M., Dieterich, D.C., et al. (2013). QuaNCAT: quantitating proteome dynamics in primary cells. Nat Methods *10*, 343–346. https://doi.org/10.1038/nmeth.2401 PMID - 23474466.

di Jeso, B., Park, Y., Ulianich, L., Treglia, A.S., Urbanas, M.L., High, S., and Arvan, P. (2005). Mixed-Disulfide Folding Intermediates between Thyroglobulin and Endoplasmic Reticulum Resident Oxidoreductases ERp57 and Protein Disulfide Isomerase. Mol Cell Biol *25*, 9793–9805. https://doi.org/10.1128/MCB.25.22.9793-9805.2005.

di Jeso, B., Morishita, Y., Treglia, A.S., Lofrumento, D.D., Nicolardi, G., Beguinot, F., Kellogg, A.P., and Arvan, P. (2014). Transient Covalent Interactions of Newly Synthesized Thyroglobulin with Oxidoreductases of the Endoplasmic Reticulum*. Journal of Biological Chemistry *289*, 11488–11496. https://doi.org/10.1074/JBC.M113.520767.

Kanou, Y., Hishinuma, A., Tsunekawa, K., Seki, K., Mizuno, Y., Fujisawa, H., Imai, T., Miura, Y., Nagasaka, T., Yamada, C., et al. (2007). Thyroglobulin Gene Mutations Producing Defective Intracellular Transport of Thyroglobulin Are Associated with Increased Thyroidal Type 2 Iodothyronine Deiodinase Activity. J Clin Endocrinol Metab *92*, 1451–1457. https://doi.org/10.1210/JC.2006-1242.

Karagöz, G.E., Acosta-Alvear, D., and Walter, P. (2019). The Unfolded Protein Response: Detecting and Responding to Fluctuations in the Protein-Folding Capacity of the Endoplasmic Reticulum. Cold Spring Harb Perspect Biol a033886. https://doi.org/10.1101/cshperspect.a033886 PMID - 30670466.

Kiick, K.L., Weberskirch, R., and Tirrell, D.A. (2001). Identification of an expanded set of translationally active methionine analogues in Escherichia coli. FEBS Lett *502*, 25–30. https://doi.org/10.1016/S0014-5793(01)02657-6.

Kim, P.S., and Arvan, P. (1995). Calnexin and BiP act as sequential molecular chaperones during thyroglobulin folding in the endoplasmic reticulum. J Cell Biol *128*, 29–38. https://doi.org/10.1083/JCB.128.1.29.

Kim, B., Arcos, S., Rothamel, K., Jian, J., Rose, K.L., McDonald, W.H., Bian, Y., Reasoner, S., Barrows, N.J., Bradrick, S., et al. (2020). Discovery of Widespread Host

Protein Interactions with the Pre-replicated Genome of CHIKV Using VIR-CLASP. Mol Cell *78*, 624-640.e7. https://doi.org/10.1016/j.molcel.2020.04.013.

Kim, P.S., Kim, K.R., and Arvan, P. (1993). Disulfide-linked aggregation of thyroglobulin normally occurs during nascent protein folding. American Journal of Physiology-Cell Physiology *265*, C704–C711. https://doi.org/10.1152/ajpcell.1993.265.3.c704 PMID - 8214027.

Kim, P.S., Kwon, O.Y., and Arvan, P. (1996). An endoplasmic reticulum storage disease causing congenital goiter with hypothyroidism. J Cell Biol *133*, 517–527. https://doi.org/10.1083/jcb.133.3.517.

Kuo, C.C., Chiang, A.W.T., Baghdassarian, H.M., and Lewis, N.E. (2021). Dysregulation of the secretory pathway connects Alzheimer's disease genetics to aggregate formation. Cell Syst *12*, 873-884.e4. https://doi.org/10.1016/J.CELS.2021.06.001.

Lamriben, L., Graham, J.B., Adams, B.M., and Hebert, D.N. (2016). N-Glycan-based ER Molecular Chaperone and Protein Quality Control System: The Calnexin Binding Cycle. Traffic *17*, 308–326. https://doi.org/10.1111/tra.12358 PMID - 26676362.

Lang, K., and Chin, J.W. (2014). Cellular Incorporation of Unnatural Amino Acids and Bioorthogonal Labeling of Proteins. Chem Rev *114*, 4764–4806. https://doi.org/10.1021/cr400355w.

Li, J., Vranken, J.G. van, Vaites, L.P., Schweppe, D.K., Huttlin, E.L., Etienne, C., Nandhikonda, P., Viner, R., Robitaille, A.M., Thompson, A.H., et al. (2020). TMTpro reagents: a set of isobaric labeling mass tags enables simultaneous proteome-wide measurements across 16 samples. Nat Methods *17*, 399–404. https://doi.org/10.1038/s41592-020-0781-4 PMID - 32203386.

Liang, J.R., Lingeman, E., Ahmed, S., and Corn, J.E. (2018). Atlastins remodel the endoplasmic reticulum for selective autophagy. Journal of Cell Biology *217*, 3354–3367. https://doi.org/10.1083/JCB.201804185.

Liang, J.R., Lingeman, E., Luong, T., Ahmed, S., Muhar, M., Nguyen, T., Olzmann, J.A., and Corn, J.E. (2020). A Genome-wide ER-phagy Screen Highlights Key Roles of Mitochondrial Metabolism and ER-Resident UFMylation. Cell *180*, 1160-1177.e20. https://doi.org/10.1016/j.cell.2020.02.017.

Lobingier, B.T., Hüttenhain, R., Eichel, K., Miller, K.B., Ting, A.Y., von Zastrow, M., and Krogan, N.J. (2017). An Approach to Spatiotemporally Resolve Protein Interaction Networks in Living Cells. Cell *169*, 350-360.e12. https://doi.org/10.1016/j.cell.2017.03.022.

Ma, Y., McClatchy, D.B., Barkallah, S., Wood, W.W., and Yates, J.R. (2017). HILAQ: A Novel Strategy for Newly Synthesized Protein Quantification. J Proteome Res *16*, 2213–2220. https://doi.org/10.1021/acs.jproteome.7b00005 PMID - 28437088.

Ma, Y., McClatchy, D.B., Barkallah, S., Wood, W.W., and Yates, J.R. (2018). Quantitative analysis of newly synthesized proteins. Nat Protoc *13*, 1744–1762. https://doi.org/10.1038/S41596-018-0012-Y.

Marinko, J.T., Wright, M.T., Schlebach, J.P., Clowes, K.R., Heintzman, D.R., Plate, L., and Sanders, C.R. (2021). Glycosylation limits forward trafficking of the tetraspan membrane protein PMP22. Journal of Biological Chemistry *296*. https://doi.org/10.1016/J.JBC.2021.100719.

McClatchy, D.B., Ma, Y., Liu, C., Stein, B.D., Martínez-Bartolomé, S., Vasquez, D., Hellberg, K., Shaw, R.J., and Yates, J.R. (2015). Pulsed Azidohomoalanine Labeling in Mammals (PALM) Detects Changes in Liver-Specific LKB1 Knockout Mice. J Proteome Res *14*, 4815–4822. https://doi.org/10.1021/acs.jproteome.5b00653 PMID - 26445171.

McDonald, E.F., Sabusap, C.M.P., Kim, M., and Plate, L. (2022). Distinct proteostasis states drive pharmacologic chaperone susceptibility for Cystic Fibrosis Transmembrane Conductance Regulator misfolding mutants. Mol Biol Cell https://doi.org/10.1091/mbc.E21-11-0578.

McGilvray, P.T., Anghel, S.A., Sundaram, A., Zhong, F., Trnka, M.J., Fuller, J.R., Hu, H., Burlingame, A.L., and Keenan, R.J. (2020a). An ER translocon for multi-pass membrane protein biogenesis. Elife *9*, 1–43. https://doi.org/10.7554/ELIFE.56889.

McGilvray, P.T., Anghel, S.A., Sundaram, A., Zhong, F., Trnka, M.J., Fuller, J.R., Hu, H., Burlingame, A.L., and Keenan, R.J. (2020b). An ER translocon for multi-pass membrane protein biogenesis. Elife *9*, 1–43. https://doi.org/10.7554/ELIFE.56889.

Menon, S., Lee, J., Abplanalp, W.A., Yoo, S.-E., Agui, T., Furudate, S., Kim, P.S., and Arvan, P. (2007). Oxidoreductase Interactions Include a Role for ERp72 Engagement with Mutant Thyroglobulin from the rdw/rdw Rat Dwarf. Journal of Biological Chemistry *282*, 6183–6191. https://doi.org/10.1074/jbc.M608863200.

Munden, A., Wright, M.T., Han, D., Tirgar, R., Plate, L., and Nordman, J.T. (2022). Identification of replication fork-associated proteins in Drosophila embryos and cultured cells using iPOND coupled to quantitative mass spectrometry. Sci Rep *12*, 1–11. https://doi.org/10.1038/s41598-022-10821-9.

Needham, P.G., Guerriero, C.J., and Brodsky, J.L. (2019). Chaperoning Endoplasmic Reticulum-Associated Degradation (ERAD) and Protein Conformational Diseases. Cold Spring Harb Perspect Biol a033928. https://doi.org/10.1101/cshperspect.a033928 PMID - 30670468.

Okuda-Shimizu, Y., and Hendershot, L.M. (2007). Characterization of an ERAD pathway for nonglycosylated BiP substrates, which require Herp. Mol Cell *28*, 544–554. https://doi.org/10.1016/J.MOLCEL.2007.09.012.

Pardo, V., Vono-Toniolo, J., Rubio, I.G.S., Knobel, M., Possato, R.F., Targovnik, H.M., Kopp, P., and Medeiros-Neto, G. (2009). The p.A2215D Thyroglobulin Gene Mutation Leads to Deficient Synthesis and Secretion of the Mutated Protein and Congenital Hypothyroidism with Wide Phenotype Variation. J Clin Endocrinol Metab *94*, 2938–2944. https://doi.org/10.1210/jc.2009-0150.

Perez Verdaguer, M., Zhang, T., Surve, S., Paulo, J.A., Wallace, C., Watkins, S.C., Gygi, S.P., and Sorkin, A. (2022). Time-resolved proximity labeling of protein networks

associated with ligand-activated EGFR. Cell Rep *39*, 110950. https://doi.org/10.1016/J.CELREP.2022.110950/ATTACHMENT/0568B930-8965-47D5-BC4E-950606E2E486/MMC8.XLSX.

Petelski, A.A., Emmott, E., Leduc, A., Huffman, R.G., Specht, H., Perlman, D.H., and Slavov, N. (2021). Multiplexed single-cell proteomics using SCoPE2. Nat Protoc *16*, 5398–5425. https://doi.org/10.1038/s41596-021-00616-z.

Phillips, S.L., Soderblom, E.J., Bradrick, S.S., and Garcia-Blanco, M.A. (2016). Identification of Proteins Bound to Dengue Viral RNA In Vivo Reveals New Host Proteins Important for Virus Replication. MBio *7*. https://doi.org/10.1128/mBio.01865-15.

Piette, B.L., Alerasool, N., Lin, Z.-Y., Lacoste, J., Lam, M.H.Y., Qian, W.W., Tran, S., Larsen, B., Campos, E., Peng, J., et al. (2021). Comprehensive interactome profiling of the human Hsp70 network highlights functional differentiation of J domains. Mol Cell https://doi.org/10.1016/j.molcel.2021.04.012 PMID - 33957083.

Pohl, C., and Dikic, I. (2019). Cellular quality control by the ubiquitin-proteasome system and autophagy. Science (1979) *366*, 818–822. https://doi.org/10.1126/science.aax3769 PMID - 31727826.

Pshezhetsky, A. v., and Hinek, A. (2011). Where catabolism meets signalling: neuraminidase 1 as a modulator of cell receptors. Glycoconjugate Journal 2011 28:7 *28*, 441–452. https://doi.org/10.1007/S10719-011-9350-5.

Rizzolo, K., and Houry, W.A. (2019). Multiple functionalities of molecular chaperones revealed through systematic mapping of their interaction networks. Journal of Biological Chemistry *294*, 2142–2150. https://doi.org/10.1074/JBC.TM118.002805.

Rizzolo, K., Huen, J., Kumar, A., Phanse, S., Vlasblom, J., Kakihara, Y., Zeineddine, H.A., Minic, Z., Snider, J., Wang, W., et al. (2017). Features of the Chaperone Cellular Network Revealed through Systematic Interaction Mapping. Cell Rep *20*, 2735–2748. https://doi.org/10.1016/j.celrep.2017.08.074 PMID - 28903051.

Ryuzono, S., Takase, R., Oishi, K., Ikeda, A., Chigwechokha, P.K., Funahashi, A., Komatsu, M., Miyagi, T., and Shiozaki, K. (2016). Lysosomal localization of Japanese medaka (Oryzias latipes) Neu1 sialidase and its highly conserved enzymatic profiles with human. Gene *575*, 513–523. https://doi.org/10.1016/J.GENE.2015.09.028.

Sabusap, C.M., Wang, W., McNicholas, C.M., Chung, W.J., Fu, L., Wen, H., Mazur, M., Kirk, K.L., Collawn, J.F., Hong, J.S., et al. (2016). Analysis of cystic fibrosis–associated P67L CFTR illustrates barriers to personalized therapeutics for orphan diseases. JCI Insight *1*. https://doi.org/10.1172/jci.insight.86581.

Sirbu, B.M., Couch, F.B., Feigerle, J.T., Bhaskara, S., Hiebert, S.W., and Cortez, D. (2011). Analysis of protein dynamics at active, stalled, and collapsed replication forks. Genes Dev *25*, 1320–1327. https://doi.org/10.1101/gad.2053211.

Smith, M.D., Harley, M.E., Kemp, A.J., Wills, J., Lee, M., Arends, M., Kriegsheim, A. von, Behrends, C., and Wilkinson, S. (2018). CCPG1 Is a Non-canonical Autophagy

855 Cargo Receptor Essential for ER-Phagy and Pancreatic ER Proteostasis. Dev Cell *44*,
856 217-232.e11. https://doi.org/10.1016/j.devcel.2017.11.024 PMID - 29290589.

857 Song, H., Orr, A., Duan, M., Merz, A.J., and Wickner, W. (2017). Sec17/Sec18 act
858 twice, enhancing membrane fusion and then disassembling cis-SNARE complexes.
859 Elife *6*. https://doi.org/10.7554/ELIFE.26646.

860 Taipale, M., Krykbaeva, I., Koeva, M., Kayatekin, C., Westover, K.D., Karras, G.I., and
861 Lindquist, S. (2012). Quantitative Analysis of Hsp90-Client Interactions Reveals Princi-
862 ples of Substrate Recognition. Cell *150*, 987–1001.
863 https://doi.org/10.1016/j.cell.2012.06.047 PMID - 22939624.

864 Taipale, M., Tucker, G., Peng, J., Krykbaeva, I., Lin, Z.-Y., Larsen, B., Choi, H., Berger,
865 B., Gingras, A.-C., and Lindquist, S. (2014). A Quantitative Chaperone Interaction Net-
866 work Reveals the Architecture of Cellular Protein Homeostasis Pathways. Cell *158*,
867 434–448. https://doi.org/10.1016/j.cell.2014.05.039.

868 Taldone, T., Wang, T., Rodina, A., Pillarsetty, N.V.K., Digwal, C.S., Sharma, S., Yan, P.,
869 Joshi, S., Pagare, P.P., Bolaender, A., et al. (2020). A Chemical Biology Approach to
870 the Chaperome in Cancer—HSP90 and Beyond. Cold Spring Harb Perspect Biol *12*,
871 a034116. https://doi.org/10.1101/cshperspect.a034116.

872 Thompson, A., Wölmer, N., Koncarevic, S., Selzer, S., Böhm, G., Legner, H., Schmid,
873 P., Kienle, S., Penning, P., Höhle, C., et al. (2019). TMTpro: Design, Synthesis, and Ini-
874 tial Evaluation of a Proline-Based Isobaric 16-Plex Tandem Mass Tag Reagent Set.
875 Anal Chem *91*, 15941–15950. https://doi.org/10.1021/acs.analchem.9b04474 PMID -
876 31738517.

877 Tokunaga, F., Brostrom, C., Koide, T., and Arvan, P. (2000). Endoplasmic reticulum
878 (ER)-associated degradation of misfolded N-linked glycoproteins is suppressed upon in-
879 hibition of ER mannosidase I. Journal of Biological Chemistry *275*, 40757–40764.
880 https://doi.org/10.1074/jbc.m001073200 PMID - 10984471.

881 Tsai, C.-F., Zhao, R., Williams, S.M., Moore, R.J., Schultz, K., Chrisler, W.B., Pasa-
882 Tolic, L., Rodland, K.D., Smith, R.D., Shi, T., et al. (2020). An Improved Boosting to Am-
883 plify Signal with Isobaric Labeling (iBASIL) Strategy for Precise Quantitative Single-cell
884 Proteomics. Molecular & Cellular Proteomics *19*, 828–838.
885 https://doi.org/10.1074/mcp.RA119.001857.

886 Vij, N., Fang, S., and Zeitlin, P.L. (2006). Selective inhibition of endoplasmic reticulum-
887 associated degradation rescues DeltaF508-cystic fibrosis transmembrane regulator and
888 suppresses interleukin-8 levels: therapeutic implications. J Biol Chem *281*, 17369–
889 17378. https://doi.org/10.1074/JBC.M600509200.

890 Vranka, J.A., Sakai, L.Y., and Bächinger, H.P. (2004). Prolyl 3-Hydroxylase 1, Enzyme
891 Characterization and Identification of a Novel Family of Enzymes. Journal of Biological
892 Chemistry *279*, 23615–23621. https://doi.org/10.1074/JBC.M312807200.

893 Wong, M.Y., and Shoulders, M.D. (2019). Targeting defective proteostasis in the colla-
894 genopathies. Curr Opin Chem Biol *50*, 80–88.
895 https://doi.org/10.1016/J.CBPA.2019.02.021.

896 Wright, M.T., and Plate, L. (2021). Revealing functional insights into ER proteostasis
897 through proteomics and interactomics. Exp Cell Res *399*.
898 https://doi.org/10.1016/J.YEXCR.2020.112417.

899 Wright, M.T., Kouba, L., and Plate, L. (2021). Thyroglobulin Interactome Profiling De-
900 fines Altered Proteostasis Topology Associated With Thyroid Dyshormonogenesis. Mo-
901 lecular & Cellular Proteomics *20*, 100008. https://doi.org/10.1074/mcp.ra120.002168
902 PMID - 33208410.

903 Zhang, X., Smits, A.H., van Tilburg, G.B.A., Ovaa, H., Huber, W., and Vermeulen, M.
904 (2018). Proteome-wide identification of ubiquitin interactions using UbIA-MS. Nature
905 Protocols 2018 13:3 *13*, 530–550. https://doi.org/10.1038/nprot.2017.147.

906 Zhao, C., Slevin, J.T., and Whiteheart, S.W. (2007). Cellular functions of NSF: Not just
907 SNAPs and SNAREs. FEBS Lett *581*, 2140–2149. https://doi.org/10.1016/J.FEB-
908 SLET.2007.03.032.

909 Zhou, H.J., Wang, J., Yao, B., Wong, S., Djakovic, S., Kumar, B., Rice, J., Valle, E., So-
910 riano, F., Menon, M.K., et al. (2015). Discovery of a First-in-Class, Potent, Selective,
911 and Orally Bioavailable Inhibitor of the p97 AAA ATPase (CB-5083). J Med Chem *58*,
912 9480–9497. https://doi.org/10.1021/ACS.JMEDCHEM.5B01346.

913

914 **STAR*METHODS**

915

916 KEY RESOURCES TABLE

REAGENT or RESOURCE	SOURCE	IDENTIFIER
Antibodies		
KDEL	Enzo Life Sciences	ADI-SPA-827
M2-FLAG	Sigma Aldrich	F1804
PDIA4	Protein Tech	14712-1-AP
TG	Proteintech	21714-1-AP
GAPDH	GeneTex	GTX627408
Tubulin-Rhodamine	BioRad	12004165
Goat anti-mouse Star-bright700	Bio-Rad	12004158
Goat anti-rabbit IRDye800	LI-COR	926-32211
Chemicals, Peptides, & Recombinant Proteins		
NMS-873	Cayman Chemical	17674
CB-5083	Cayman Chemical	19311

ML-240	Cayman Chemical	17373
dithiobis(succinimidyl propionate) (DSP)	Thermo Scientific	22585
2-(4-((Bis((1-(*tert*-butyl)-1*H*-1,2,3-triazol-4-yl)methyl)amino)methyl)-1*H*-1,2,3-triazol-1-yl)acetic acid (BTTAA)	Click Chemistry Tools	1236
Carboxytetramethylrhodamine (TAMRA)-Azide-Polyethylene Glycol (PEG)-Desthiobiotin	BroadPharm	BP-22475
DharmaFECT1 Transfection Reagent	Dharmacon	T-2001
Lipofectamine 3000	Invitrogen	L3000
G1 Anti-DYKDDDDK affinity resin	GenScript	L00432
High-Capacity Streptavidin agarose resin	Pierce	20357
Commercial Assays		
Nano-Glo Luciferase Assay System	Promega	N1110
Deposited Data		
Proteomics RAW and analyzed data	This study	
Experimental Models: Cell Lines		
Human HEK293 Flp-In	Thermo Fisher	R75007
Fischer Rat Thyroid (FRT) Flp-In	(Sabusap et al., 2016)	N/A
Recombinant DNA		
Tg-FLAG - pcDNA3.1+/C-(K)-DYK	Genscript	OHu20241
pcDNA5/FRT	(Sabusap et al., 2016)	N/A
pOG44	(Sabusap et al., 2016)	N/A
pcDNA5/FRT-Tg-FLAG	This study	N/A
pcDNA5/FRT-Tg-NLuc	This study	N/A
pMRX-INU-TEX264-FLAG	Addgene	128258
pMRX-INU-SEC62-FLAG	Addgene	128263
Sequence-Based Reagents		
Site-Directed Mutagenesis Primers	This study	See Table S1
qPCR Primers	This study	See Table S1

siGenome Cherry Picked Library	Dharmacon	See Table S6
Software		
Bio-Rad Image Lab	Bio-Rad	https://www.bio-rad.com/en-us/product/image-lab-software
Prism 9	GraphPad	https://www.graphpad.com/scientific-software/prism/
Proteome Discoverer 2.4	Thermo Fisher	https://www.thermofisher.com
CFX Maestro	Bio-Rad	https://www.bio-rad.com/en-us/product/cfx-maestro-software-for-cfx-real-time-pcr-instruments
FlowJo	BD Biosciences	https://www.flowjo.com/solutions/flowjo/downloads

917

918 LEAD CONTACT AND MATERIALS AVAILABILITY

919

920 All unique/stable reagents generated, including plasmids and cell lines are available

921 from the Lead Contact, Lars Plate (lars.plate@vanderbilt.edu) with a complete Materials

922 Transfer Agreement.

923

924 **METHOD DETAILS**

925

926 **Plasmid Production and Antibodies**

927 Tg-FLAG in pcDNA3.1+/C-(K)-DYK plasmid was purchased from Genscript (Clone ID

928 OHu20241). The Tg-FLAG gene was then amplified and assembled with an empty

929 pcDNA5/FRT expression vector using a HiFi DNA assembly kit (New England BioLabs,

930 E2621). This plasmid then underwent site-directed mutagenesis to produce pcDNA5-

931 C1264R-Tg-FLAG, and pcDNA5-A2234D-Tg-FLAG plasmids (Table S1).

932 An oligonucleotide fragment encoding Nanoluciferase (NLuc) was ordered from
933 Genewiz. To generate pcDNA5/FRT-Tg-NLuc plasmids the Tg gene was amplified from
934 the pcDNA5/FRT-Tg-FLAG plasmid and assembled with the NLuc fragment using a HiFi
935 DNA assembly kit (New England BioLabs). To generate the respective mutant construct
936 plasmids for A2234D and C1264R Tg, site directed mutagenesis was performed using a
937 Q5 polymerase (New England BioLabs). All oligonucleotide sequences can be found in
938 Table S1.
939
940 **Cell Line Engineering**
941 FRT cells were cultured in Ham's F-12, Coon's Modification (F12) media (Sigma, cat.
942 No. F6636) supplemented with 5% fetal bovine serum (FBS), and 1% penicillin
943 (10,000U) / streptomycin (10,000 µg/mL). To generate FRT flp-Tg-FT cells, $5x10^5$ cells
944 cultured for 1 day were cotransfected with 2.25 µg flp recombinase pOG44 plasmid and
945 0.25 µg of FT-Tg pcDNA5 plasmid using Lipofectamine 3000. Cells were then cultured
946 in media containing Hygromycin B (100 µg/mL) to select site-specific recombinants. Re-
947 sistant clonal lines were sorted into single cell colonies using flow cytometry and
948 screened for FT-Tg expression (Table S1 and Figures S1A-S1D).
949 To generate HEK293 flp-Tg-NLuc cells, $5x10^5$ cells cultured for 1 day were co-
950 transfected with 2.25 µg flp recombinase pOG44 plasmid and 0.25 µg of NLuc-Tg
951 pcDNA5 plasmid using Lipofectamine 3000. Cells were then cultured in media contain-
952 ing Hygromycin B (100 µg/mL) to select site specific recombinants. Polyclonal lines

953 were screened for Tg-NLuc expression and furimazine substrate turnover (Figures S1E-
954 S1K).
955
956 **Time-Resolved Interactome Profiling**
957 Fully confluent 15cm tissue culture plates of FRT cells were used. Cells were washed
958 with phosphate buffered saline (PBS) and depleted of methionine by incubating with
959 methionine free Dulbecco's Modified Eagle Medium (DMEM) supplemented with 5% di-
960 alyzed fetal bovine serum (FBS), 1% L-glutamine (2mM final concentration), 1% L-cys-
961 teine (200 µM final concentration), and 1% penicillin (10,000U) / streptomycin (10,000
962 µg/mL) for 30 minutes. Cells were then pulse labeled with Hpg-enriched DMEM supple-
963 mented with with 1% Hpg (200µM final concentration), 5% dialyzed FBS, 1% L-gluta-
964 mine (200mM final concentration), 1% L-cysteine (200µM), and 1% penicillin (10,000U)
965 / streptomycin (10,000 µg/mL) for 1 hour. After pulse labeling cells were washed with
966 F12 media containing 10-fold excess methionine (2mM final concentration). Cells were
967 then cultured in normal F12 media supplemented with 5% FBS and chased for the
968 specified time-points. Cells were harvested by washing with PBS and then crosslinked
969 with 0.5mM DSP in PBS at 37ºC for 10 minutes. Crosslinking was quenched by the ad-
970 dition of 100mM Tris pH 7.5 at 37ºC for 5 minutes. Lysates were prepared by lysing in
971 Radioimmunoprecipitation assay (RIPA) buffer (50mM Tris pH 7.5, 150mM NaCl, 0.1%
972 SDS, 1% Triton X-100, 0.5% deoxycholate) with protease inhibitor cocktail (Roche,
973 4693159001). Protein concentration was normalized to 1mg/mL using a BCA assay
974 (Thermo Scientific, 23225) and cell lysates underwent click reactions with the addition of

975 0.8mM copper sulfate (diluted from a 20mM stock in water), 1.6mM BTTAA (diluted
976 from a 40mM stock in water), 5mM sodium ascorbate (diluted from a 100mM stock in
977 water), and 100uM TAMRA-Azide-PEG-Desthiobiotin ligand (diluted from a 5mM stock
978 in DMSO). Samples were allowed to react at 37º for 1 hour while shaking at 750rpm.
979 Cell lysates were then precleared on 4B sepharose beads (Sigma, 4B200) at 4°C for 1
980 hour while rocking. Precleared lysates were immunoprecipitated with G1 Anti-
981 DYKDDDDK affinity resin overnight at 4°C while rocking. Resin was washed four times
982 with RIPA buffer, and proteins were eluted twice in 100µL immunoprecipitation elution
983 buffer (2% SDS in PBS) by heating at 95°C for 5 minutes. Eluted samples from FLAG
984 immunoprecipitations were then diluted with PBS to reduce the final SDS concentration
985 to 0.2%. The solutions then underwent streptavidin enrichment with high-capacity strep-
986 tavidin agarose resin (Pierce, 20359) for 2 hours at room temperature while rotating.
987 The resin was then washed with 1mL each of 1% SDS, 4M Urea, 1M sodium chloride,
988 followed by a final wash with 1% SDS (all wash buffers dissolved in PBS). Resin was
989 frozen overnight at -80ºC and samples were then eluted twice with 100µL biotin elution
990 buffer (50mM Biotin in 1% SDS in PBS) by heating at 37ºC and shaking at 750rpm for 1
991 hour. Eluted streptavidin enrichment samples were precipitated in methanol/chloroform,
992 washed three times with methanol, and air dried. Protein pellets were then resuspended
993 in 3µL 1% Rapigest SF Surfactant (Waters, 186002122) followed by the addition of
994 10µL of 50mM HEPES pH 8.0, and 34.5µL of water. Samples were reduced with 5mM
995 tris(2-carboxyethyl)phosphine (TCEP) (Sigma, 75259) at room temperature for 30
996 minutes and alkylated with 10mM iodoacetimide (Sigma, I6125) in the dark at room

997 temperature for 30 minutes. Proteins were digested with 0.5 µg of trypsin/Lys-C prote-
998 ase mix (Pierce, A40007) by incubating for 16-18 hours at 37°C and shaking at 750rpm.
999 Peptides were reacted with TMTpro 16plex reagents (Thermo Fisher, 44520) in 40% v/v
1000 acetonitrile and incubated for one hour at room temperature. Reactions were quenched
1001 by the addition of ammonium bicarbonate (0.4% w/v final concentration) and incubated
1002 for one hour at room temperature. TMT labeled samples were then pooled and acidified
1003 with 5% formic acid (Fisher, A117, v/v). Samples were concentrated using a speedvac
1004 and resuspended in buffer A (97% water, 2.9% acetonitrile, and 0.1% formic acid, v/v/v).
1005 Cleaved Rapigest SF surfactant was removed by centrifugation for 30 minutes at
1006 21,100 x g.
1007 For TRIP analysis coupled with ML-240 treatment, C1264R Tg FRT cells were
1008 processed as described above with ML-240 (10µM) supplemented in Hpg-pulse media
1009 and throughout the chase period.
1010
1011 **Liquid Chromatography – Tandem Mass Spectrometry**
1012 MudPIT microcolumns were prepared as previously described (Fonslow et al., 2012).
1013 Peptide samples were directly loaded onto the columns using a high-pressure chamber.
1014 Samples were then desalted for 30 minutes with buffer A (97% water, 2.9% acetonitrile,
1015 0.1% formic acid v/v/v). LC-MS/MS analysis was performed using an Exploris480
1016 (Thermo Fisher) mass spectrometer equipped with an Ultimate3000 RSLCnano system
1017 (Thermo Fisher). MudPIT experiments were performed with 10µL sequential injections
1018 of 0, 10, 30, 60, and 100% buffer C (500mM ammonium acetate in buffer A), followed

1019 by a final injection of 90% buffer C with 10% buffer B (99.9% acetonitrile, 0.1% formic
1020 acid v/v) and each step followed by a 140 minute gradient from 4% to 80% B with a flow
1021 rate of 500nL/minute on a 20cm fused silica microcapillary column (ID 100 µm) ending
1022 with a laser-pulled tip filled with Aqua C18, 3µm, 125 Å resin (Phenomenex). Elec-
1023 trospray ionization (ESI) was performed directly from the analytical column by applying
1024 a voltage of 2.2kV with an inlet capillary temperature of 275°C. Data-dependent acquisi-
1025 tion of mass spectra was carried out by performing a full scan from 400-1600m/z at a
1026 resolution of 120,000. Top-speed data acquisition was used for acquiring MS/MS spec-
1027 tra using a cycle time of 3 seconds, with a normalized collision energy of 32, 0.4m/z iso-
1028 lation window, automatic maximum injection time and 100% normalized AGC target, at
1029 a resolution of 45,000 and a defined first mass (m/z) starting at 110. Peptide identifica-
1030 tion and TMT-based protein quantification was carried out using Proteome Discoverer
1031 2.4. MS/MS spectra were extracted from Thermo Xcalibur .raw file format and searched
1032 using SEQUEST against a Uniprot rat proteome database supplemented with the hu-
1033 man thyroglobulin gene (accessed 03/2014 and containing 28860 entries). The data-
1034 base was curated to remove redundant protein and splice-isoforms. Searches were car-
1035 ried out using a decoy database of reversed peptide sequences and the following pa-
1036 rameters: 20ppm peptide precursor tolerance, 0.02 Da fragment mass tolerance, mini-
1037 mum peptide length of 6 amino acids, trypsin cleavage with a maximum of two missed
1038 cleavages, dynamic methionine modification of +15.995 Da (oxidation), dynamic protein
1039 N-terminus +42.011 Da (acetylation), -131.040 (methionine loss), -89.030 (methionine
1040 loss + acetylation), static cysteine modification of +57.0215 Da (carbamidomethylation),

1041 and static peptide N-terminal and lysine modifications of +304.2071 Da (TMTpro
1042 16plex).
1043
1044 **Immunoblotting and SDS-PAGE**
1045 Cell lysates were prepared by lysing in RIPA buffer with protease inhibitor cocktail
1046 (Roche) and protein concentrations were normalized using a BCA assay (Thermo Sci-
1047 entific). Lysates were then denatured with 1X Laemmli buffer + 100mM DTT and heated
1048 at 95°C for 5 minutes before being separated by SDS-PAGE. Samples were transferred
1049 onto poly-vinylidene difluoride (PVDF) membranes (Millipore, IPFL00010) for immunob-
1050 lotting and blocked using 5% non-fat dry milk dissolved in tris buffered saline with 0.1%
1051 Tween-20 (Fisher, BP337-100) (TBS-T). Primary antibodies were incubated either at
1052 room temperature for 2 hours, or overnight at 4°C. Membranes were then washed three
1053 times with TBS-T and incubated with secondary antibody in 5% non-fat dry milk dis-
1054 solved in TBS-T either at room temperature for 1 hour or overnight at 4°C. Membranes
1055 were washed three times with TBS-T and then imaged using a ChemiDoc MP Imaging
1056 System (BioRad). Primary antibodies were acquired from commercial sources and used
1057 at the indicated dilutions in immunoblotting buffer (5% bovine serum albumin (BSA) in
1058 Tris-buffered saline pH 7.5, 0.1% Tween-20, and 0.1% sodium azide): KDEL (1:1000),
1059 M2 anti-FLAG (1:1000), PDIA4 (1:1000), thyroglobulin (1:1000). Tubulin-Rhodamine pri-
1060 mary antibody was obtained from commercial sources and used at 1:10000 dilution in
1061 5% milk in Tris-buffered saline pH 7.5, 0.1% Tween-20 (TBS-T). Secondary antibodies
1062 were obtained from commercial sources and used at the indicated dilutions in 5% milk

1063 in TBS-T: Goat anti-mouse Star-bright700 (1:10000), Goat anti-rabbit IRDye800
1064 (1:10000).
1065
1066 **qRT-PCR**
1067 RNA was prepared from cell pellets using the Quick-RNA miniprep kit (Zymo Research).
1068 cDNA was synthesized from 500ng total cellular RNA using random hexamer primer
1069 (IDT), oligo-dT primer (IDT), and M-MLV reverse transcriptase (Promega). qPCR analy-
1070 sis was performed using iTaq Universal SYBR Green Supermix (Bio-Rad) combined
1071 with primers for genes of interest and reactions were run in 96-well plates on a Bio-Rad
1072 CFX qPCR instrument. Data analysis was then carried out in CFX Maestro (Bio-Rad).
1073 Primer sequences for genes of interest are found in Table S1.
1074
1075 **siRNA Screening Assay**
1076 Proteins previously identified as Tg interactors, and other key proteostasis network
1077 components were selected and targeted using an siGENOME SMARTpool siRNA li-
1078 brary (Dharmacon) (Wright et al., 2021). HEK293 cells stably expressing Tg-NLuc con-
1079 structs were seeded into 96-well plates at $2.5x10^4$ cells/well and transfected using Dhar-
1080 maFECT 1 following the DharmaFECT1 protocol (Dharmacon) with a 25nM siRNA con-
1081 centration. Approximately 36 hours after transfection, cells were washed with PBS and
1082 replenished with fresh DMEM media. After 4 hours, Tg-NLuc abundance in the lysate
1083 and media were measured using the nano-glo luciferase assay system according to the
1084 manufactures protocol (Promega). Four controls were included for the experiments

1085 including a non-targeting siRNA control, a siGLO fluorescent control to monitor transfec-
1086 tion efficiency, a vehicle control containing transfection reagents but lacking any siR-
1087 NAs, and a lethal TOX control. Data was median normalized across individual 96-well
1088 plates (Chung et al., 2008). Data represents two independent experiments for WT-NLuc
1089 and A2234D-NLuc, and three independent experiments for C1264R NLuc. Cutoff crite-
1090 ria for hits were set to those genes that increased or decreased Tg-NLuc abundance in
1091 lysate or media by 3σ.
1092
1093 **FRT siRNA Validation Studies**
1094 For siRNA silencing follow-up experiments, Tg FRT cells were seeded into 6-well dishes
1095 at 6.0×10^5 cells/well transfected using DharmaFECT 1 following the DharmaFECT pro-
1096 tocol (Dharmacon) with a 25nM siRNA concentration. Approximately 36 hours after
1097 transfection, cells were washed with PBS and harvested for qRT-PCR. For qRT-PCR
1098 siRNA target transcript levels were normalized to a GAPDH loading control to monitor
1099 siRNA silencing efficiency. For immunoblot analysis approximately 36 hours after trans-
1100 fection cells were washed with PBS and replenished with fresh DMEM media. After 4
1101 hours in the case of WT Tg and 8 hours in the case of C1264R or A2234D Tg, cells and
1102 media samples were harvested. Cells were lysed with 1mL of RIPA with protease inhibi-
1103 tor cocktail (Roche), and lysate and media samples were subjected to immunoprecipita-
1104 tion with G1 Anti-DYKDDDDK affinity resin overnight at 4°C while rocking. After three
1105 washes with RIPA buffer, protein samples were eluted with 3× Laemmli buffer with 100

1106 mM DTT heating at 95ºC for 5 min. Immunoblot quantification was performed using Im-
1107 age Lab Software (BioRad).
1108
1109 **^{35}S Pulse Chase Assay**
1110 Confluent 6-well dishes of FRT cells (approximately 1x10^{6}/well) were metabolically la-
1111 beled in DMEM depleted of methionine and cysteine and supplemented with EasyTag
1112 ^{35}S Protein Labeling Mix (Perkin Elmer, NEG772007MC), glutamine, penicillin/strepto-
1113 mycin, and 10% FBS at 37ºC for 30 minutes. Afterward, cells were washed twice with
1114 F12 media containing 10X methionine and cysteine, followed by a burn off period of 10
1115 minutes in normal F12 media. Cells were then chased for the respective time periods
1116 with normal F12 media, lysed with 500uL of RIPA buffer with protease inhibitor cocktail
1117 (Roche) and 10 mM DTT. Cell lysates were diluted with 500uL of RIPA buffer with pro-
1118 tease inhibitor cocktail (Roche) and subjected to immunoprecipitation with G1 anti-
1119 DYKDDDDK affinity resin overnight at 4ºC. After three washes with RIPA buffer, protein
1120 samples were eluted with 3× Laemmli buffer with 100 mM DTT heating at 95ºC for 5
1121 minutes. Eluted samples were then separated by SDS-PAGE, and gels were dried and
1122 exposed on a storage phosphor screen. Radioactive band intensity was then measured
1123 using a Typhoon Trio Imager (GE Healthcare) and quantified by densitometry in Image
1124 Lab (BioRad).
1125 For pulse chase analysis coupled with ML-240 treatment, cells were pre-treated
1126 with vehicle (0.1% DMSO) or ML-240 (10μM) for 15 minutes prior to ^{35}S pulse labeling.

1127 Vehicle (0.1% DMSO) or ML-240 (10μM) treatment was then maintained throughout the
1128 pulse labeling and chase period.
1129
1130 **VCP Pharmacological Inhibition Studies**
1131 For follow-up experiment with VCP inhibitors, confluent 6-well dishes of C1264R Tg-FT
1132 FRT cells were washed with PBS and fresh F12 media supplemented with ML-240
1133 (10μM), CB-5083 (5μM), NMS-873 (10μM), or vehicle (0.1% DMSO) was added and in-
1134 cubated for 8 hours. For WT Tg-FT cells, confluent 6-well dishes were similarly used,
1135 washed with PBS and fresh F12 media supplemented with ML-240 (10μM) or vehicle
1136 (0.1% DMSO) was added and incubated for 4 or 8 hours. Cells were lysed with 1mL of
1137 RIPA with protease inhibitor cocktail (Roche), and lysate and media samples were sub-
1138 jected to immunoprecipitation with G1 Anti-DYKDDDDK affinity resin overnight at 4°C
1139 while rocking. After three washes with RIPA buffer, protein samples were eluted with 3×
1140 Laemmli buffer with 100 mM DTT heating at 95ºC for 5 minutes. Immunoblot
1141 quantification was performed using Image Lab Software (BioRad).
1142 Viability with ML-240 was monitored using propidium iodide staining. Briefly, cells
1143 were treated with either ML-240 (10μM) or vehicle (0.1% DMSO) for 4 hours before be-
1144 ing harvested and stained with propidium iodide (1μg/mL) at room temperature for 15
1145 minutes in the dark. Cells permeabilized with 0.2% Triton were used as a positive stain-
1146 ing control. Data analysis was then carried out in FlowJo (BD Biosciences).
1147
1148 **TEX264 & Tg-NLuc Co-Immunoprecipitation Studies**

1149 HEK293 flp-Tg-NLuc cells were cultured at $1.0x10^5$ cells/well in 12-well tissue culture
1150 dishes for 1 day and transfected with either a fluorescent control, c-terminal FLAG-tag
1151 TEX264, or c-terminal FLAG-tag SEC62 using a calcium phosphate method. Confluent
1152 plates were harvested by lysing with 300uL of TNI buffer (50mM Tris pH 7.5, 150 mM
1153 NaCl, 0.5% IGEPAL CA-630 (Sigma-Aldrich)) and protease inhibitor (Roche). Lysates
1154 were sonicated for 10 minutes at room temperature and normalized using a BCA Assay
1155 (Thermo Scientific). Cell lysates were then precleared on 4B sepharose beads (Sigma,
1156 4B200) at 4°C for 1 hour while rocking, then immunoprecipitated with G1 Anti-
1157 DYKDDDDK affinity resin overnight at 4°C while rocking. Resin was washed four times
1158 with TNI buffer and resuspended in 250 µL of TNI buffer. 50 µL aliquots were taken and
1159 measured using the nano-glo luciferase assay system according to the manufactures
1160 protocol (Promega). For differential enrichment, statistical analysis was performed in
1161 Prism 9 (GraphPad) using a one-way ANOVA with post hoc Tukey's multiple testing
1162 corrections.
1163 For western blot analysis HEK293 flp-Tg-NLuc $1.0x10^6$ cells/dish in 10 cm tissue
1164 culture dishes for 1 day and transfected with either a fluorescent control, TEX264, or
1165 SEC62 using a calcium phosphate method. Cells were collected and lysed using 300
1166 µL of TNI buffer with protease inhibitor (Roche) sonicated at room temperature for 10
1167 minutes. Lysates were normalized, precleared, and immunoprecpitated as described
1168 above. Proteins were eluted using 6X Laemmli buffer + 100mM DTT, separated by
1169 SDS-PAGE and transferred to PVDF membrane (Millipore) for immunoblotting.
1170

1171 **QUANTIFICATION AND STATISTICAL ANALYSIS**

1172

1173 Mass Spectrometry Interactomics and TMT Quantification

1174 To identify Tg interactors (-) biotin pulldown vs (-) Hpg samples were processed using
1175 the DEP pipeline (Zhang et al., 2018). Enriched proteins were determined based on
1176 those with a log2 fold change of 2σ and Benjamini-Hochberg adjusted p-value (false
1177 discovery rate) of 0.05. For pathway enrichment analysis of identified proteins, EnrichR
1178 was used and GO Cellular Component and Molecular Function 2018 terms were used
1179 to differentiate secretory pathway associated proteins from background (Chen et al.,
1180 2013). For time resolved analysis, data were processed in R with custom scripts. Briefly,
1181 TMT abundances across chase samples were normalized to Tg TMT abundance as de-
1182 scribed previously and compared to (-) Hpg samples for enrichment analysis (Wright et
1183 al., 2021). Inconsistencies in the quantification of Tg bait protein were observed for rep-
1184 licate 5 of WT Tg Hpg-chase samples, likely due to sample loss during the enrichment.
1185 Hence, this replicate was excluded from further time-resolved analysis. All analysis
1186 scripts are available as described in the Data and Code Availability section.

1187

1188 **DATA AND CODE AVAILABILITY**

1189 Mass spectrometry spectrum and result files are available via ProteomeXchange under
1190 identifier PXD035681. Raw TMT quantification data is available in Table S7. Code used
1191 for data analysis and generation of figures is available at
1192 github.com/wrighmt1/2022_TRIP.

1193

1194 **Figure Legends**

1195 **Figure 1. Time-Resolved Interactome Profiling to Identify Interactions with New**

1196 **Synthesized Proteins.**

1197 (A) Key steps necessary for the TRIP workflow utilizing pulsed unnatural amino acid la-

1198 beling with Hpg (Box 1), labeled protein functionalization with CuAAC click chemistry

1199 (Box 2), global immunoprecipitation (Box 3), followed by streptavidin-biotin enrichment

1200 into time-resolved fractions (Box 4).

1201 (B-D) Western blot analysis of the two-stage purification strategy with continuous Hpg

1202 labeling. FRT cells stably expressing WT Tg were pulse-labeled with Hpg (200μM) for 4

1203 hrs and crosslinked with DSP (0.5mM) for 10 minutes to capture transient proteostasis

1204 network interactions (+ Xlink). Lysates were functionalized with a TAMRA-Azide-PEG-

1205 Desthiobiotin probe using copper catalyzed azide-alkyne cycloaddition (CuAAC) and

1206 subjected to the dual affinity purification scheme as described.

1207 (B) FLAG IP inputs as described in Box 2 in (A). Top shows fluorescence image of rho-

1208 damine labeled proteins, and bottom shows immunoblots of Tg (IB: FLAG) and interac-

1209 tors HSP90B1, HSPA5, PDIA4 and loading control GAPDH.

1210 (C) FLAG IP elutions as described in Box 3 in (A). Top shows fluorescence image of

1211 rhodamine labeled Tg and total Tg (IB: FLAG). Bottom shows immunoblots of interac-

1212 tors (HSP90B1, HSPA5, and PDIA4). Samples were then subjected to biotin pulldown.

1213 (D) Biotin pulldown elutions as described in Box 4 in (A). Top shows fluorescence image

1214 of rhodamine labeled Tg and total Tg (IB: FLAG). Bottom shows immunoblots of interac-

1215 tors (HSP90B1, HSPA5, and PDIA4).

1216

1217 **Figure 2. TRIP Temporally Resolves Tg Interactions with Protein Quality Control**

1218 **Components**

1219 (A) Workflow for TRIP protocol utilizing western blot or mass spectrometric analysis of

1220 time-resolved interactomes. Samples were pulse-labeled with Hpg (200μM final concen-

1221 tration) for 1 hour, then chased in regular media for specified time points, and cross

1222 linked with DSP (0.5mM) for 10 minutes to capture transient proteoastasis network in-

1223 teractions. Lysates were functionalized with a TAMRA-Azide-PEG-Desthiobiotin probe

1224 using copper catalyzed azide-alkyne cycloaddition (CuAAC). Chase samples were pro-

1225 cessed through the dual affinity purification TRIP workflow and processed for mass

1226 spectrometry or western blot analysis. (-) Hpg samples were unlabeled and served as

1227 negative controls.

1228 (B and C) TRIP western blot analysis of WT Tg-FT (B) and C1264R Tg-FT (C). Samples

1229 were processed as described above in (A). FLAG IP Input panel shows immunoblot of

1230 Tg (IB:FLAG), and interactors HSP90B1, HSPA5, PDIA4 and loading control GAPDH.

1231 Biotin pulldown elution panel shows fluorescence image of rhodamine labeled Tg and

1232 immunoblot of Tg interactors HSP90B1 and HSPA5. Validated Tg interactors show

1233 higher and delayed enrichment with the misfolded C1264R Tg mutant in (C) compared

1234 to WT in (B).

1235 (D and E) Plots showing the log2 fold change enrichment of select Tg interactors

1236 HSPA5 and PDIA4 compared across constructs. Samples were processed as described

1237 above in (A) and analyzed by mass spectrometry. Temporal trends from western blot
1238 analysis are recapitulated with mass spectrometry analysis.
1239
1240 **Figure 3. TRIP Identifies Altered Temporal Dynamics Associated with Tg Pro-**
1241 **cessing**
1242 (A) TMTpro labeling scheme for TRIP experiments including a (-) Hpg control channel to
1243 identify enriched interactors and a (-) Biotin pulldown channel to act as a booster (or
1244 carrier). Chase samples are pulse labeled with Hpg (200µM) for 1 hour. Cells are then
1245 harvested at specified time points and cross linked with DSP (0.5mM) for 10 minutes to
1246 capture transient proteoastasis network interactions. Lysates are functionalized with a
1247 TAMRA-Azide-PEG-Desthiobiotin probe using copper catalyzed azide-alkyne cycloaddi-
1248 tion (CuAAC). Chase samples are processed through the dual affinity purification TRIP
1249 workflow and processed for mass spectrometry. (-) biotin pulldown samples were col-
1250 lected after the first FLAG co-IP and serve as positive control and booster channel. (-)
1251 Hpg samples were processed through the dual affinity purification TRIP workflow ,in-
1252 cluding 3 hr chase period, serving as negative controls to assess background.
1253 (B) Venn diagram showing the overlap in proteostasis components identified as Tg in-
1254 teractors here compared to our previous data set (Wright et al., 2021; Zhang et al.,
1255 2018). (-) biotin pulldown vs (-) Hpg samples were used to identify Tg interactors in FRT
1256 cells.
1257 (C) Plot showing the relative pathway enrichment for Hsp70/90 assisted folding & chap-
1258 eroning interactors with WT, A2234D, or C1264R Tg constructs. For this and all

1259 subsequent panels, the average log2 fold change enrichment value across time points
1260 for a given interactor were used to scale data. Positive enrichment was scaled from 0 to
1261 1. Lines represent the median scaled enrichment for the group of interactors and
1262 shades correspond to the first and third quartile range. All source data for this and sub-
1263 sequent panels can be found in Table S6.
1264 (D) Heatmap showing the relative enrichment for individual Hsp70/90 assisted folding &
1265 chaperoning interactors with WT, A2234D, or C1264R Tg constructs. Relative enrich-
1266 ment scaled as described above in (C). Source data found in Table S6.
1267 (E) Heatmap showing the relative enrichment for select membrane biogenesis interac-
1268 tors with WT and C1264R Tg constructs.
1269 (F) Plot showing the relative pathway enrichment for disulfide/redox processing interac-
1270 tors with WT, A2234D, or C1264R Tg constructs. Relative enrichment scaled and plot-
1271 ted as described above in (C). Lines and shades are defined as in in (C).
1272 (G) Heatmap showing the relative enrichment for individual disulfide/redox processing
1273 interactors with WT, A2234D, or C1264R Tg constructs.
1274 (H) Heatmap showing the relative enrichment for select prolyl isomerization & hydrox-
1275 ylation interactors with WT, A2234D, or C1264R Tg constructs.
1276 (I) Heatmap showing the relative enrichment for select glycan processing Tg interactors
1277 with WT, A2234D, or C1264R Tg constructs.
1278 (J) Plot showing the relative pathway enrichment for proteasomal degradation Tg in-
1279 teractors with WT, A2234D, or C1264R Tg constructs. Lines and shades are defined as
1280 in in (C).

1281 (K) Heatmap showing the relative enrichment for select proteasomal degradation Tg in-
1282 teractors with WT, A2234D, or C1264R Tg constructs.
1283 (L) Heatmap showing the relative enrichment for select autophagy Tg interactors with
1284 WT, A2234D, or C1264R Tg constructs.
1285
1286 **Figure 4. siRNA Screening Deconvolutes Interactions and Key Regulators of Con-**
1287 **struct Specific Tg Processing**
1288 (A) siRNA screening workflow utilizing NLuc-tagged Tg to monitor lysate and media
1289 abundance. Approximately 36 hours after transfection with 25nM siRNAs cells were re-
1290 plenished with fresh media and Tg-NLuc abundance in lysate and media was measured
1291 after 4 hours using the nano-glo luciferase assay system.
1292 (B) Violin plots showing the relative Tg-NLuc abundance changes in lysate with siRNA
1293 knockdown of select genes. Tg-NLuc abundance in lysate was measured 4 hours after
1294 replenishing with fresh media using the nano-glo luciferase assay system. Cutoff criteria
1295 for hits were set to those genes that increased or decreased Tg-NLuc abundance in ly-
1296 sate or media by 3σ. Hits are labeled within the plot. Source data found in Table S7.
1297 (C) Violin plots showing the relative Tg-NLuc abundance changes in media with siRNA
1298 knockdown of select genes. Sample processing and cutoff criteria to identify hits are de-
1299 scribed above in (B). Source data found in Table S7.
1300
1301 **Figure 5. Trafficking and Degradation Factors Selectively Regulate Tg Processing**
1302 **in FRT cells**

1303 (A and B) Western blot analysis of WT Tg-FT secretion from FRTR cells after transfec-
1304 tion with select siRNAs hits from initial screening data set. Cells were transfected with
1305 25nM siRNAs for 36 hours, media exchanged and conditions for 4 hrs, Tg-FT was im-
1306 munoprecipitated from lysate and media samples, and Tg-FT amounts were analyzed
1307 via immunoblotting.
1308 (C and D) Western blot analysis of C1264R Tg-FT secretion from FRT cells transfected
1309 with select siRNA hits from the initial screening data set. Samples were processed as in
1310 (A). All statistical testing performed using an unpaired student's t-test with Welch's cor-
1311 rection. *p<0.05, **p<0.005, ***p<0.0005.
1312
1313 **Figure 6. Mutant Tg is Selectively Enriched with the ER-phagy Receptor TEX264**
1314 (A) Schematic for western blot and NLuc analysis for identifying TEX264-Tg interac-
1315 tions. HEK293T cells stably expression WT or mutant Tg-NLuc were transfected with
1316 FLAG-tagged ER-phagy receptors TEX264, SEC62, or GFP control. After FLAG Co-IP,
1317 samples were analyzed using the using the nano-glo luciferase assay system or im-
1318 munoblot analysis to monitor Tg enrichment.
1319 (B) Luminescence data from FLAG-CoIP and nano-glo luciferase analysis. Tg is selec-
1320 tively enriched with TEX264 compared to GFP fluorescent control, or SEC62. Mutant Tg
1321 exhibits higher enrichment compared to WT. Data represented as mean ± SEM. Statisti-
1322 cal testing was performed using a one-way ANOVA with post hoc Tukey's multiple test-
1323 ing corrections, *p<0.05, **p<0.005, ***p<0.0005.

1324 (C) Western blot analysis of FLAG Co-IP samples. Top panel shows IP inputs and bot-
1325 tom panel IP elutions with Tg (IB:Tg), ER-phagy receptors (IB:FLAG and IB:TEX264)
1326 and loading control Tubulin. Tg is selectively enriched with TEX264 compared to GFP
1327 fluorescent control, or SEC62, with C1264R Tg exhibiting higher enrichment compared
1328 to WT.
1329
1330 **Figure 7. Pharmacological VCP Inhibition Selectively Rescues C1264R Tg Secre-**
1331 **tion through Interactome Remodeling**
1332 (A and B) Western blots analysis of C1264R Tg-FT FTR cells treated with VCP inhibi-
1333 tors ML-240 (10μM), CB-5083 (5μM), NMS-873 (10μM), or vehicle (0.1% DMSO) for 8
1334 hours. Lysate and media samples were subjected to immunoprecipitation and analyzed
1335 via immunoblotting. Data is normalized to the median C1264R Tg-FT abundance of
1336 DMSO treated samples. Data represented as mean ± SEM. Statistical testing performed
1337 using an unpaired student's t-test with Welch's correction, *$p<0.05$, **$p<0.005$,
1338 ***$p<0.0005$.
1339 (C and D) Western blots analysis of WT Tg-FT FTR cells treated with ML-240 for 4 and
1340 8 hours. Lysate and media samples were processed and analyzed as described above
1341 (A and B). Data is normalized to the median WT Tg-FT abundance of DMSO treated
1342 samples. Data representation and statistical testing as in (B)
1343 (E) ^{35}S Pulse-chase analysis of C1264R Tg-FT FTR cells with ML-240 treatment. Cells
1344 were pre-treated with ML-240 or DMSO for 15 minutes prior to pulse labeling with ^{35}S

1345 for 30 minutes and chased for 4 hours with DMSO or ML-240 treatment. Data is repre-
1346 sented as mean ± SEM. Full data panel available in Figure S7C and S7D.
1347 (F) ^{35}S Pulse chase analysis of WT Tg-FT FRT cells with ML-240 (10µM) treatment.
1348 Samples processed as described above in (E). Data is represented as mean ± SEM.
1349 Full data panel available in Figure S7E and S7F.
1350 (G-L) TRIP analysis showing the relative enrichment for select Tg interactors across
1351 proteostasis pathways between untreated and ML-240 (10µM) treated C1264R Tg.
1352 Cells were treated with ML-240 (10µM) and analyzed utilizing the TRIP workflow. The
1353 average log2 fold change enrichment values across time points for a given interactor
1354 are used to scale data. Positive enrichment values were scaled from 0 to 1, while nega-
1355 tive enrichment values were scaled from 0 to -1. The enrichment is shown for Glycan
1356 Processing (G and H), Hsp70/90 Assisted Folding (I-J), and Disulfide/Redox Processing
1357 (K-L). Aggregate pathway enrichment is displayed in (G), (I), and (J), where lines repre-
1358 sent the median scaled enrichment for the group of interactors and shades correspond
1359 to the first and third quartile range. Heatmaps with individual enrichments of interactors
1360 is shown in (H), (J), and (L). Full data panel available in Figure S8A-S8C.
1361

Figures

Figure 1

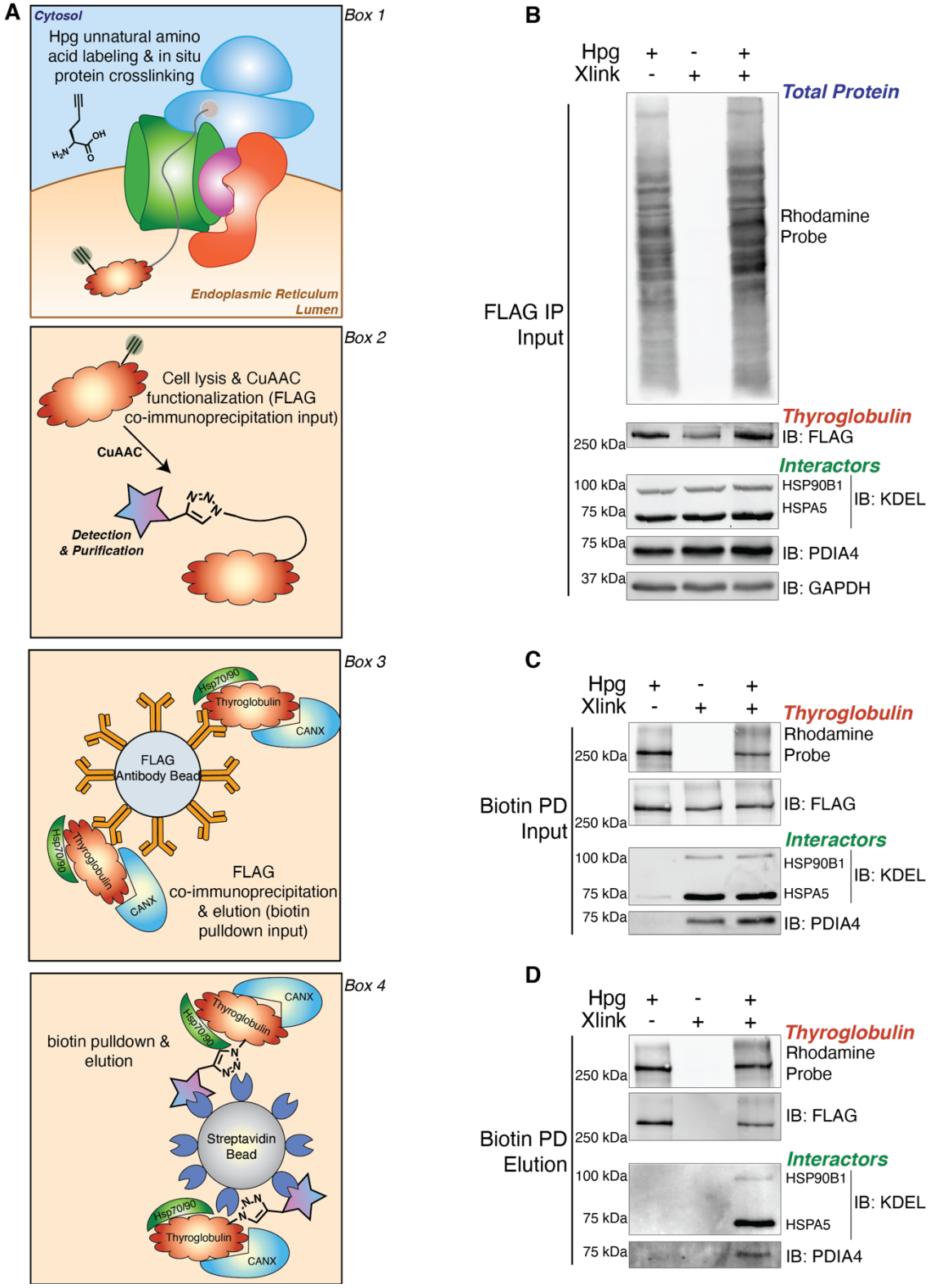

Figure 2.

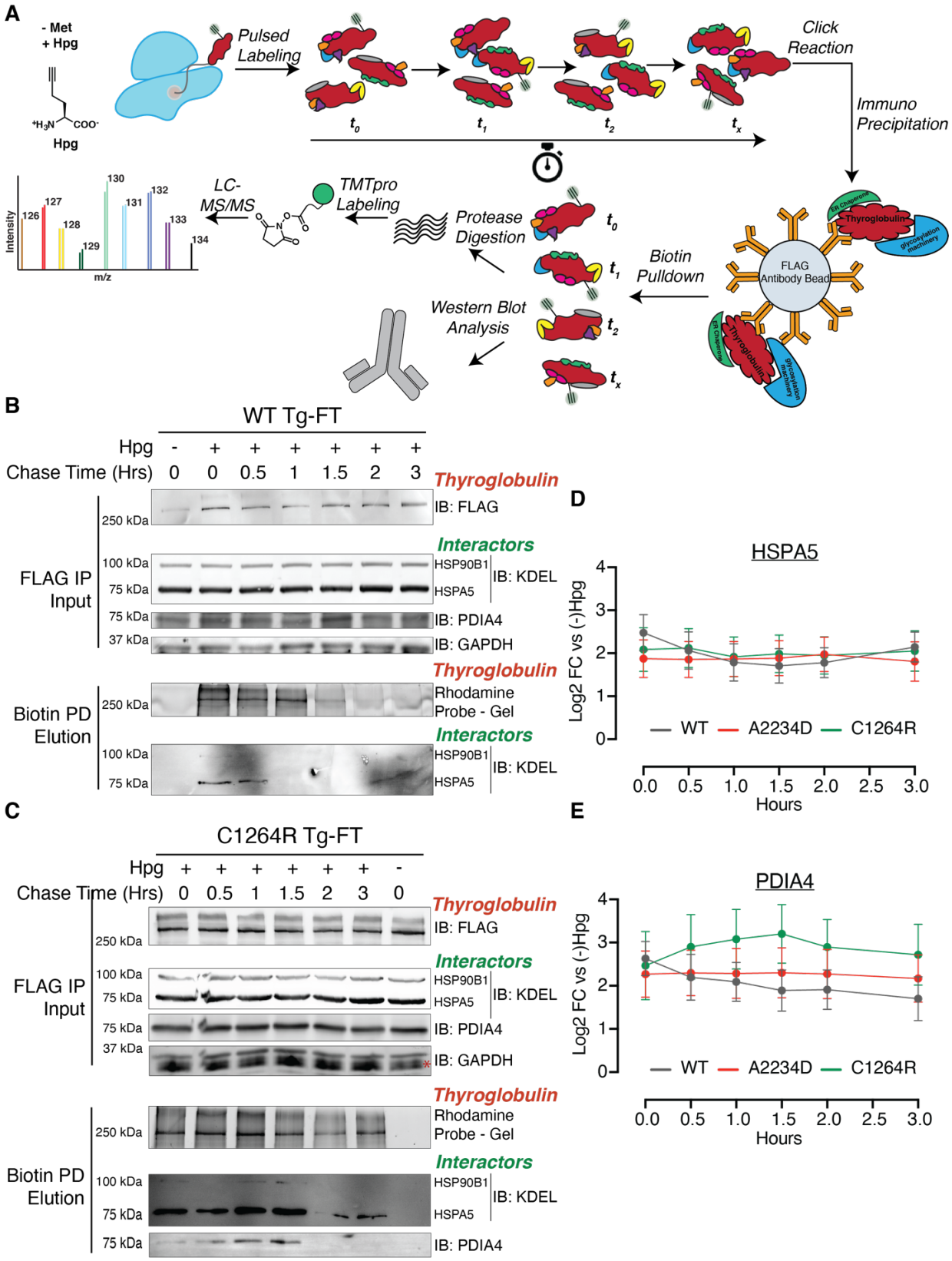
A
- Met
+ Hpg
Hpg
Pulsed Labeling
Click Reaction
Immuno Precipitation
Biotin Pulldown
FLAG Antibody Bead
Thyroglobulin
ER Chaperone
glycosylation machinery
Protease Digestion
TMTpro Labeling
LC-MS/MS
Intensity
m/z
Western Blot Analysis
B
WT Tg-FT
Hpg - + + + + + +
Chase Time (Hrs) 0 0 0.5 1 1.5 2 3
Thyroglobulin
IB: FLAG
Interactors
HSP90B1
HSPA5
IB: KDEL
IB: PDIA4
IB: GAPDH
FLAG IP Input
Biotin PD Elution
Rhodamine Probe - Gel
C
C1264R Tg-FT
Hpg + + + + + + -
Chase Time (Hrs) 0 0.5 1 1.5 2 3 0
D
HSPA5
Log2 FC vs (-)Hpg
WT
A2234D
C1264R
Hours
E
PDIA4

Figure 3.

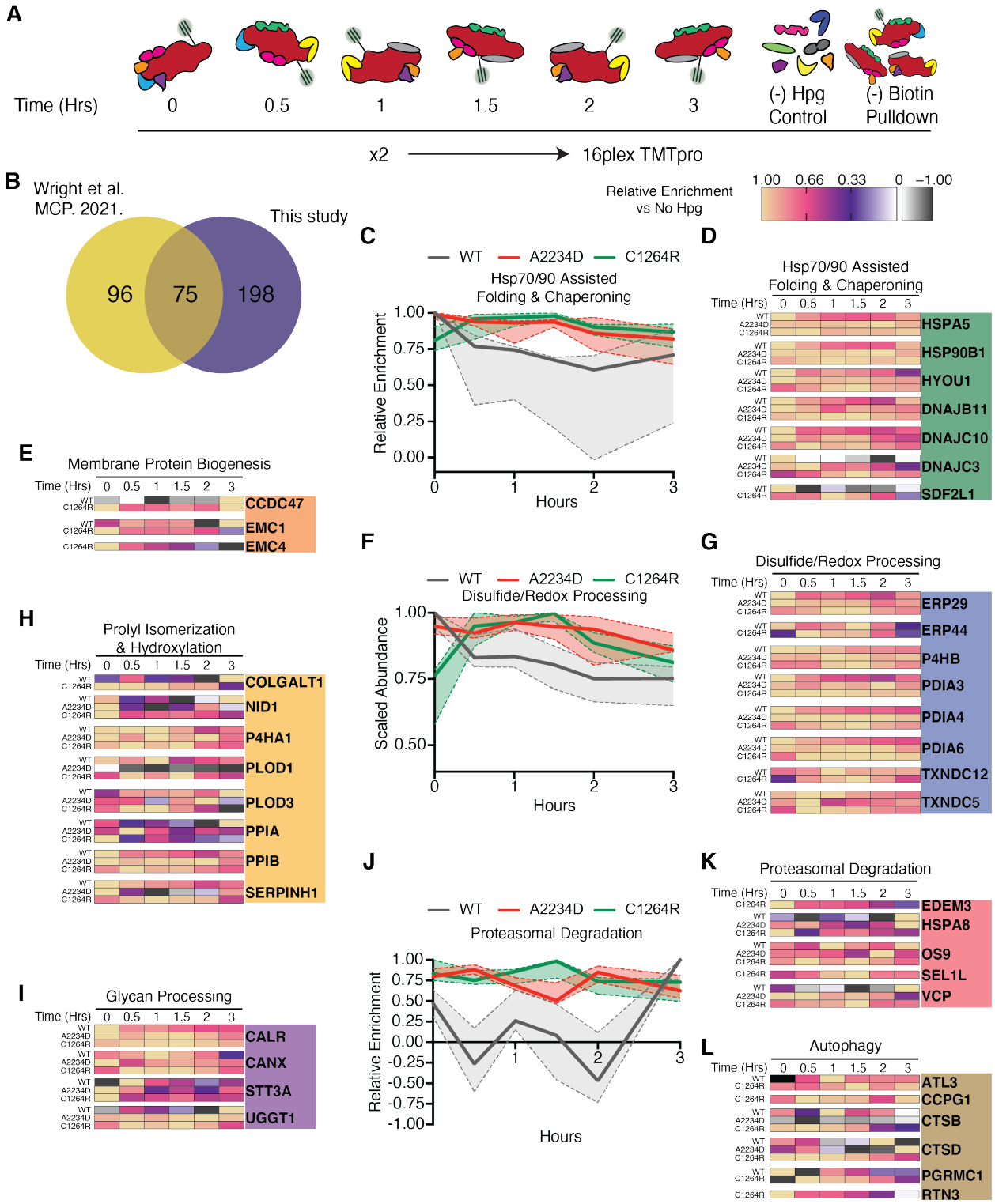
A
Time (Hrs)
0
0.5
1
1.5
2
3
(-) Hpg Control
(-) Biotin Pulldown
x2
16plex TMTpro
B
Wright et al. MCP. 2021.
This study
96
75
198
Relative Enrichment vs No Hpg
1.00 0.66 0.33 0 −1.00
C
WT A2234D C1264R
Hsp70/90 Assisted Folding & Chaperoning
Relative Enrichment
Hours
D
Hsp70/90 Assisted Folding & Chaperoning
HSPA5
HSP90B1
HYOU1
DNAJB11
DNAJC10
DNAJC3
SDF2L1
E
Membrane Protein Biogenesis
CCDC47
EMC1
EMC4
F
Disulfide/Redox Processing
Scaled Abundance
Hours
G
Disulfide/Redox Processing
ERP29
ERP44
P4HB
PDIA3
PDIA4
PDIA6
TXNDC12
TXNDC5
H
Prolyl Isomerization & Hydroxylation
COLGALT1
NID1
P4HA1
PLOD1
PLOD3
PPIA
PPIB
SERPINH1
I
Glycan Processing
CALR
CANX
STT3A
UGGT1
J
Proteasomal Degradation
K
Proteasomal Degradation
EDEM3
HSPA8
OS9
SEL1L
VCP
L
Autophagy
ATL3
CCPG1
CTSB
CTSD
PGRMC1
RTN3

Figure 4.

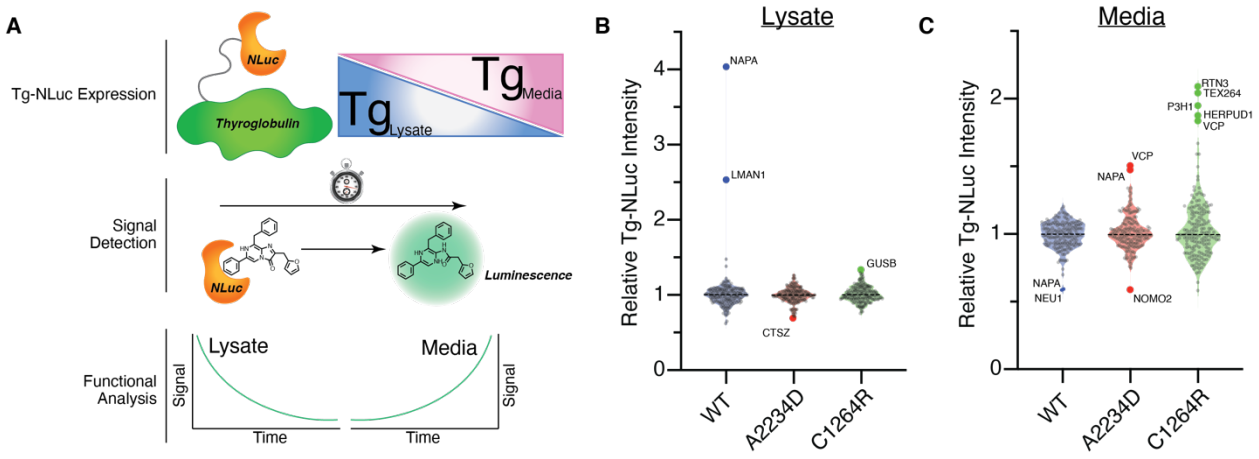
A
Tg-NLuc Expression
NLuc
Thyroglobulin
Tg Media
Tg Lysate
Signal Detection
NLuc
Luminescence
Functional Analysis
Lysate
Media
Signal
Time
Time
Signal
B
Lysate
Relative Tg-NLuc Intensity
NAPA
LMAN1
CTSZ
GUSB
WT
A2234D
C1264R
C
Media
Relative Tg-NLuc Intensity
RTN3
TEX264
P3H1
HERPUD1
VCP
VCP
NAPA
NAPA
NEU1
NOMO2
WT
A2234D
C1264R

Figure 5.

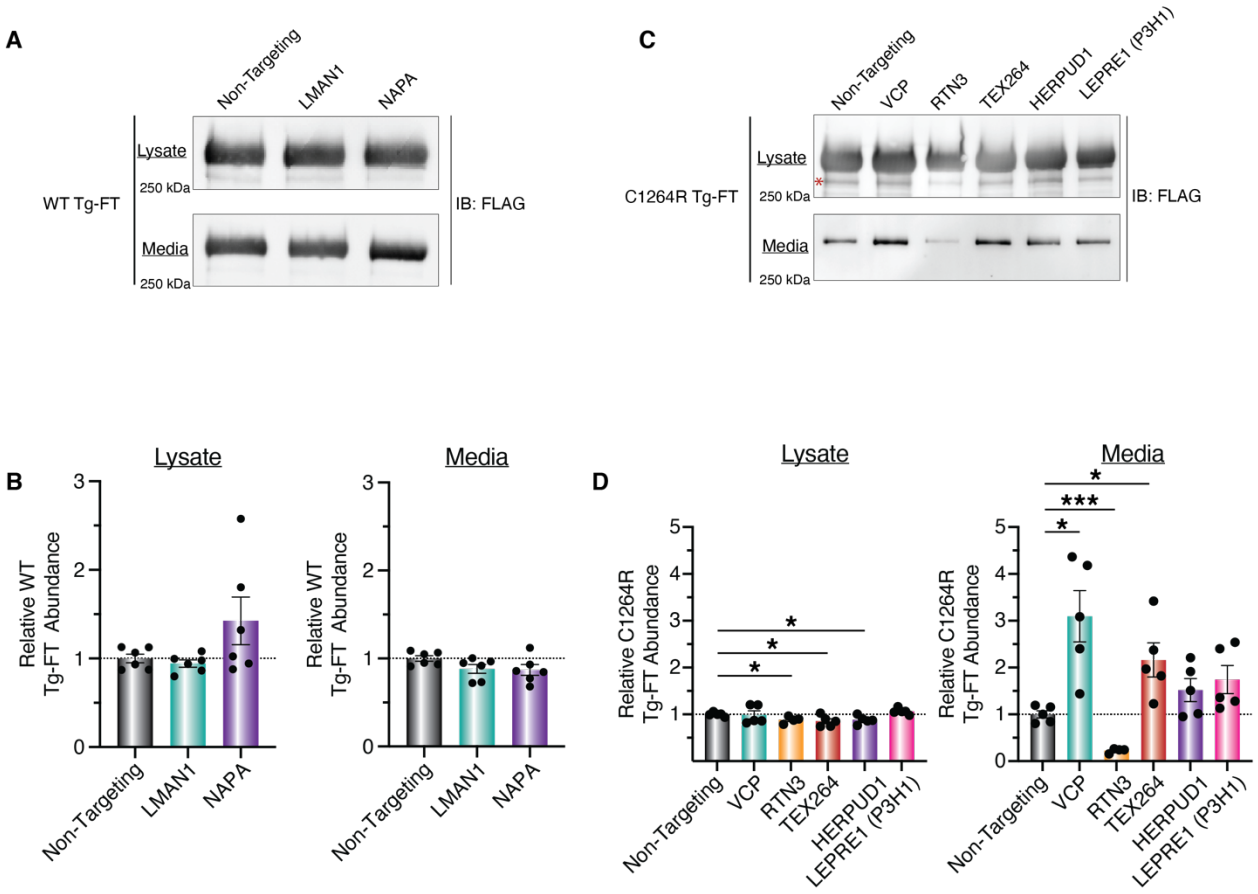
A
Non-Targeting
LMAN1
NAPA
Lysate
250 kDa
WT Tg-FT
Media
250 kDa
IB: FLAG
C
Non-Targeting
VCP
RTN3
TEX264
HERPUD1
LEPRE1 (P3H1)
Lysate
C1264R Tg-FT
250 kDa
Media
250 kDa
IB: FLAG
B
Lysate
Media
Relative WT Tg-FT Abundance
Non-Targeting
LMAN1
NAPA
D
Lysate
Media
Relative C1264R Tg-FT Abundance
Non-Targeting
VCP
RTN3
TEX264
HERPUD1
LEPRE1 (P3H1)

Figure 6.

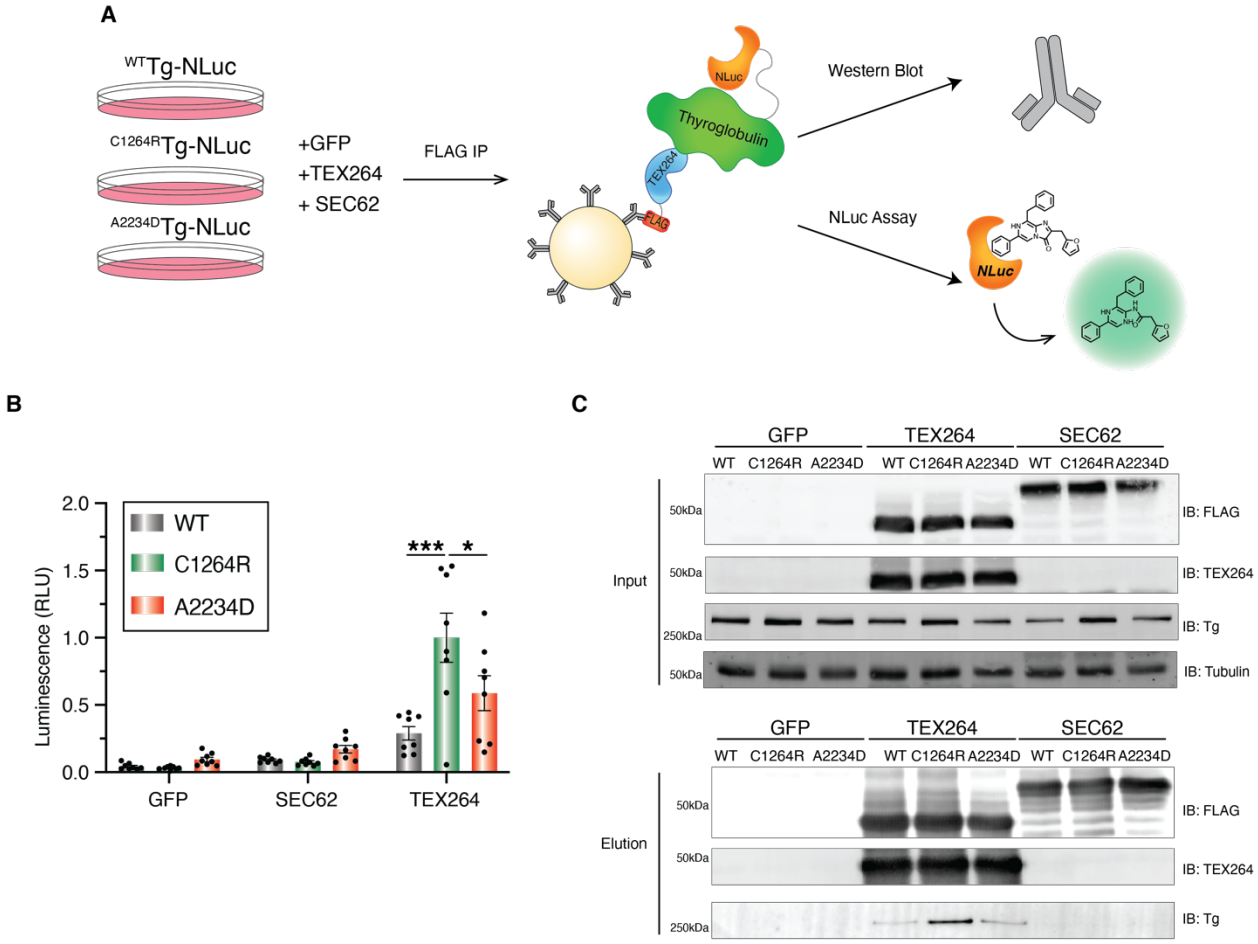
A
WTTg-NLuc
C1264RTg-NLuc
A2234DTg-NLuc
+GFP
+TEX264
+ SEC62
FLAG IP
NLuc
Thyroglobulin
TEX264
FLAG
Western Blot
NLuc Assay
NLuc
B
Luminescence (RLU)
2.0
1.5
1.0
0.5
0.0
WT
C1264R
A2234D
***
*
GFP
SEC62
TEX264
C
GFP
TEX264
SEC62
WT C1264R A2234D WT C1264R A2234D WT C1264R A2234D
Input
50kDa
IB: FLAG
IB: TEX264
250kDa
IB: Tg
IB: Tubulin
Elution

Figure 7.

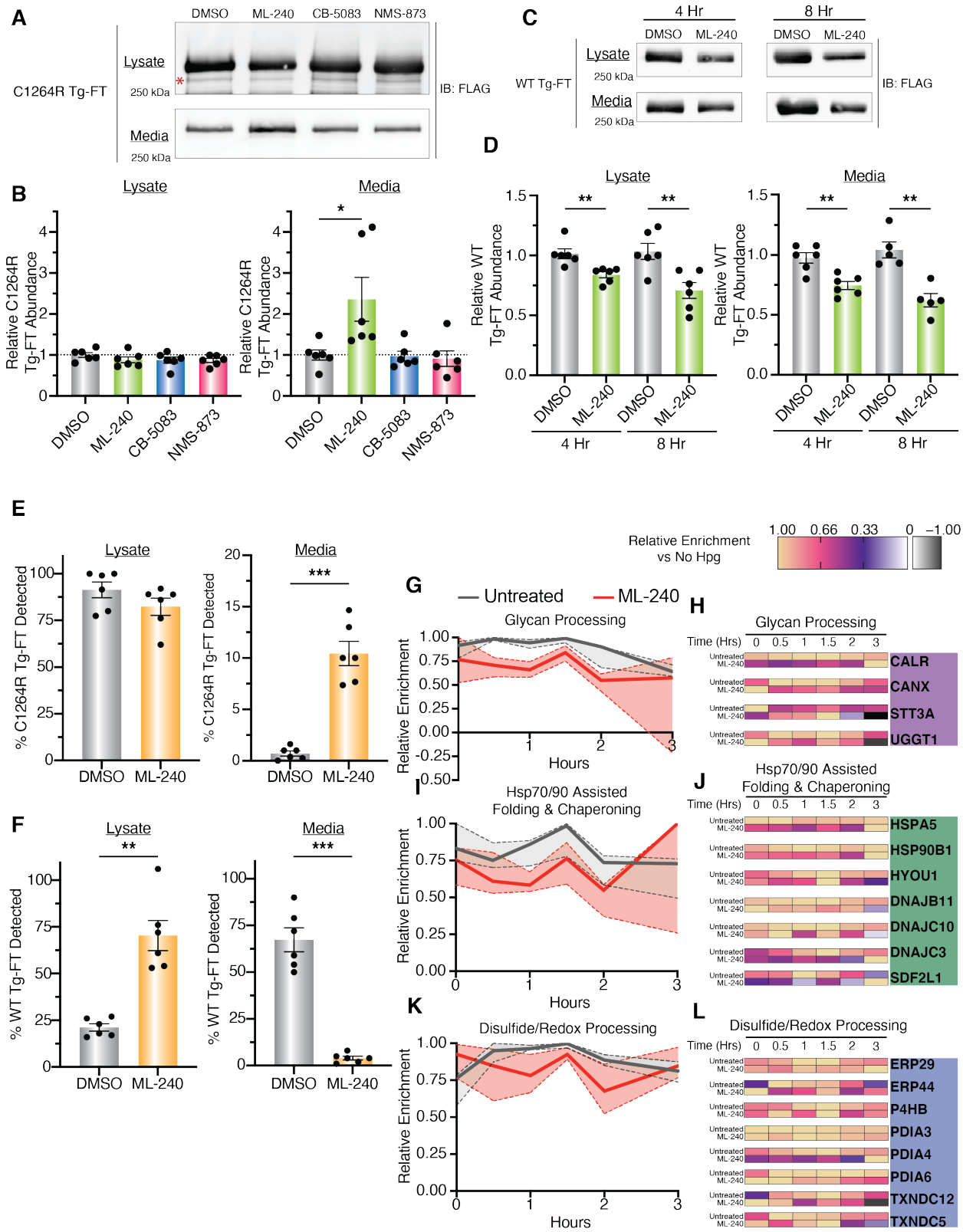
A
DMSO
ML-240
CB-5083
NMS-873
C1264R Tg-FT
Lysate
250 kDa
Media
250 kDa
IB: FLAG
B
Lysate
Media
Relative C1264R Tg-FT Abundance
DMSO
ML-240
CB-5083
NMS-873
C
4 Hr
8 Hr
WT Tg-FT
D
Relative WT Tg-FT Abundance
E
% C1264R Tg-FT Detected
F
% WT Tg-FT Detected
Relative Enrichment vs No Hpg
1.00
0.66
0.33
0
−1.00
G
Untreated
ML-240
Glycan Processing
Relative Enrichment
Hours
H
Time (Hrs)
CALR
CANX
STT3A
UGGT1
I
Hsp70/90 Assisted Folding & Chaperoning
J
HSPA5
HSP90B1
HYOU1
DNAJB11
DNAJC10
DNAJC3
SDF2L1
K
Disulfide/Redox Processing
L
ERP29
ERP44
P4HB
PDIA3
PDIA4
PDIA6
TXNDC12
TXNDC5